Alma Mater Studiorum · University of Bologna

School of Science
Department of Physics and Astronomy
Master Degree in Physics

Scalar Stars and Effective Field Theory

Supervisor:
Prof. Michele Cicoli

Co-supervisor:
Dr. Francisco Manuel Soares Verissimo Gil Pedro

Submitted by:
Pablo Díaz Calzadilla

Academic Year 2019/2020

Abstract

The axion is one of the favored candidates to form the cold dark matter in the universe. This pseudo-scalar field may form compact objects called axion stars, whose physics is well captured by means of non-relativistic effective field theory coupled to Newtonian gravity. The interplay between gradient energy, self-interactions and gravity gives rise to both dilute and dense axion stars. While the existence of the *dilute axion stars* is well established, the situation is more complicated in the case of the so-called *dense axion stars*, an extra physically stable solution of the system of differential equations describing the dynamics of the axion field in the regime where self-interactions play an important role. The existence of the dense axion stars has not been settled in the literature.

In this thesis, we discuss first the appropriate non-relativistic formalism for the study of these clumps by means of the various *non-relativistic reductions* found in the literature. We analyze the stability, for different sizes and number of particles, of these objects considering quartic self-interaction potentials. This allows us to corroborate the results for these cases already presented by other authors. We also go beyond the simplest case, by analyzing more complicated potentials describing with higher precision the axion self-interactions. By employing the correct non-relativistic axion effective field theory we show that the dense branch is an artefact of the non-relativistic reduction procedure.

Contents

Chapter 1

Introduction

The relevance of the scalar fields in our description of the universe has grown over the years. The most relevant one among them is the Higgs field. In the mechanism suggested by Higgs [1] and Anderson [2] for the introduction of mass in a theory (the so-called *Higgs mechanism*, see Chapter 10 in [3] for further details). Crucial for a theoretical completeness of the Standard Model of particle physics (SM), its existence was experimentally demonstrated in 2012 [4].

However, there are several reasons for the existence of other spin-0 fields in nature. One of them is the so-called *inflaton* [5, 6]. This scalar field is central in the most accepted solution for the *fine tunning problems* of conventional Big Bang theory, this is, the high homogeneity in the different causally disconnected patches of the early universe and the necessity of a very concrete initial conditions to obtain the current structure of our universe at large scales [7]. These issues are fixed by introducing an exponential expansion period called *inflation*. The simplest models describing this early period include a single scalar field ϕ, the already mentioned inflaton, whose dynamics are fully determined by the potential $V(\phi)$ describing its self-interactions. Its particular shape continues being discussed and diverse models have been introduced, as *natural inflation*, whose potential shows a cosine shape, or others with more complicated forms as the Coleman-Weinberg potential [8].

Scalar can be also relevant in the context of cold dark matter (CDM). Since dark matter was postulated by F. Zwicky in 1933 [9] and S. Smith in 1936 [10], many experimental evidences of its existence have been accumulating, such as the flat galactic rotation curves (see [11] and references therein), the Chandra satellite X-rays observations [12] or the circular gravitational lensing images [13]. However, the particle physics origin of the CDM remains unknown. Currently, the possible candidates include incoherent spin-0 particles or coherent oscillations of scalar fields, to name a few. In the former category we have the weakly interactive massive particles (WIMP) or their decaying products and in the latter the bosonic collective motion of particles such as the axion. Both of them arise in different extensions of the SM as remarkable solutions for

diverse issues. Unification of couplings and the hierarchy problem, for instance, require certain kinds of WIMP. On the other hand, the strong CP problem and the unification with gravity within string theory are deeply related with axions.

So far, the direct detection of the WIMP in the different colliders or through other kind of experiments has been unsuccessful in its most highly motivated regime of the parameter space. Nonetheless, in the case of axions, its more obvious regime has not been fully explored up to now, although different experiments in this direction are planned. Henceforth we are going to center our analysis in the axion.

An example of this pseudo-scalar field, whose existence is solid from a theoretical point of view, is the so-called *QCD axion*. Particularly, its existence was suggested as a consequence of the introduction of the *Peccei-Quinn mechanism*, the most accepted solution to the so-called *strong CP problem* of QCD. More in detail, the spontaneous breaking of the *Peccei-Quinn* symmetry $U(1)_{PQ}$ at a scale of the axion decay constant $f \sim 10^{11}$ GeV, leads to the appearance of this pseudo-Goldstone boson [14, 15].

Nevertheless, during the rest of this discussion, we will not be focused on this axion specifically. In our case we are going to consider always a generic axion field in diverse momentum regimes giving a more general view, easy to particularize in future work for a specific case, such as the already mentioned QCD axion.

To be more concrete, our analysis will be centred in certain hypothetical objects composed by axions, the so-called *axion stars*. They are included in a bigger category of compact clumps, the *solitons*, which are physically stable solutions of the equations of motion of scalar fields in general. They are divided in two subcategories. If their stability is ensured by the existence of a topological charge, we talk about *topological solitons*, such as vortexes or kinks. If not, we have the so-called *non-topological solitons*. In the later case, the stability is ensured by the conservation of a Noether charge. A slightly different kind of object is also included here, the so-called *non-topological pseudo-solitons*, which are just meta-stable instead. This kind of objects are long-lived due to approximate symmetries, as we are going to discuss later.

In particular, among the diverse possible non-topological (pseudo-)solitons, we will consider the ones composed by just one single scalar field or *scalar stars*, which are also divided in

- Complex Scalar Stars:

  Solitons composed by a single complex scalar field with a $\mathcal{L}$ showing an explicit $U(1)$ symmetry, which ensures their stability.

  - ◇ *Q-balls*: Complex scalar stars arising in the regime in which gravity is negligible and the gradient energy is compensated by attractive self-interactions.
  - ◇ *Bosons stars*: Complex scalar stars appearing in the regime in which gravity is relevant and compensates the gradient energy. Self-interactions could be also present and their intensity is linked with the mass of these compact objects,

in such a way that weak self-interaction lead us to the so-called *Mini-bosons stars*

– Real Scalar Stars:

Pseudo-solitons composed by a single real scalar field. Although their $\mathcal{L}$ does not present any conserved quantity, they are extremely long-lived, as shown in many numerical simulations [16].

◇ *I-balls/Oscillons*: Real scalar stars arising in the regime in which gravity is negligible and the gradient energy is compensated by attractive self-interactions. A typical example of an object of this category are the so called *Moduli stars* [17, 18], whose scalar field is a *moduli field*, common in string theory.

◇ *Oscillatons*: Real scalar stars appearing in the regime in which gravity is relevant and compensates the gradient energy. Self-interactions are also present and will play a crucial role in the meta-stability regimes of these objects. Axion stars are considered in this category.

The meta-stability of real scalar stars is at first sight problematic. As the Lagrangian does not present any evident symmetry we could expect no formation of such a compact objects. This statement is refuted by numerical simulations which do not only support their existence, but also prove them really long-lived.

This issue was studied in detail at [19]. In their effective field theory, Mukaida et al. separate relativistic and non-relativistic modes of the axion field. Then the former are integrated out and the resulting non-relativistic effective field theory shows an approximate global $U(1)$ symmetry. Now, we have two conserved quantities: the energy and charge associated to this already mentioned symmetry. The justification for this treatment is also given, as it is demonstrated that the decay rate induced by the imaginary part is much slower that the frequency of the typical solutions for the QCD axion. Thus, at each time step, we can safely regard its energy and charge as conserved quantities, discussing its decay as an adiabatic process.

More in detail, these compact objects are nothing but a type of Bose-Einstein condensates (BEC) or *axion BEC* in our case. The existence of this kind of axion condensates has been suggested by various authors [20, 21] with their stability being linked with the interplay between self-interactions and gravity. Even though they are expected to be formed in the early universe, leaving a signature in the form of background gravitational waves (GW), their appearance at later times is not discarded, being in this case part of the current CDM forming the universe.

Concerning the characteristics of this axion BEC, its most relevant properties are linked with the fact that we are not talking about a conventional BEC with a long range order but about a type of *localized clump* [22]. This BEC formation is directly associated

with the fact that the ground state is a bound state due to the attractive nature of either gravitation and self-interactions. In [20, 23] the idea of gravitational interactions leading axions in the early universe to thermal equilibrium is introduced. This thermalization may produce these BEC and also drive them locally towards the lowest-energy accessible state.

We study the stability of these condensates considering the quartic potential, going also beyond this simplest case, repeating our analysis for more complicated potentials describing with higher precision the axion self-interactions.

The outline of our discussion is as follows: In Chapter 2 we will review the proper formalisms for the study of the axion field in the diverse momentum regimes paying special attention the diverse *non-relativistic reductions* present in the literature. In Section 3.1 the equations describing the dynamics of the axion will be introduced. In Section 3.2 and 3.3, we will consider the simplest self-interaction potentials and study the stability regimes of the axion stars in these cases. Finally, in Section 3.4, we will consider more complicated and accurate non-relativistic self-interaction potentials, allowing us to probe the dense branch of solutions and to show that it is an artefact of the non-relativistic reduction procedure.

Chapter 2

Non-relativistic Reductions

The theoretical framework for the proper study of axions, depends mainly on the momentum scale. For momenta small compared with the axion decay constant (f) but higher the axion mass (m_a), the axion is represented by an elementary quantum real Lorentz scalar field $\phi(x)$. In this interval, it presents local self-interactions generated by a periodic potential $\mathcal{V}(\phi)$ and it is perfectly described by means of relativistic effective field theory.

On the other hand, when we consider a momentum scale below the axion mass m_a, a non-relativistic effective field theory treatment (NREFT), also called *axion EFT*, captures in a simpler way its properties. Here instead of a real field, the axion will be represented by an elementary complex scalar field $\psi(x)$, with self-interactions generated by an effective potential $\mathcal{V}(\psi^*\psi)$.

Even if the last regime is most relevant one for our discussion, we are going to review first the former regime and the relativistic effective field theory describing the axion field on it, as it will be the starting point for the axion EFT.

After that, we will be fully concentrated in the lower momentum regime, paying special attention to the non-relativistic reduction, this is, to how could we obtain our complex scalar field $\psi(x)$ from the relativistic real scalar field $\phi(x)$ in an accurate manner. Along with this non-relativistic reduction, the specific shape of the already mentioned effective potential will be obtained. At last, we will consider different formulations proposed by diverse authors, which have been shown equivalent, for the calcultation of valid non-relativistic reductions.

One of the main applications of this NREFT treatment, concerns axionic dark matter. The non-relativistic axions produced by the vacuum misalignment mechanism presents huge occupation numbers, so they are commonly described by means of a real-valued classical field $\phi(\mathbf{r}, t)$ that evolves according to relativistic field equations. Nevertheless, if axions form a BEC, they will be readily treated by means of a complex-valued classical field $\psi(\mathbf{r}, t)$ with an evolution described by the non-relativistic field equations of axion EFT. In general, many of the theoretical problems concerning axionic dark matter could

be faced more appropriately by means of axion EFT.

2.1 Relativistic Axion Field Theory

As said, for momenta between the axion decay constant f and the axion mass m_a, the axion could be studied easily by means of relativistic field theory treatment, represented by a real scalar field $\phi(x)$ with self-interactions mediated by a *relativistic axion potential* $\mathcal{V}(\phi)$. The Lagrangian density describing this scalar field and its self interactions in this interval will be then

$$\mathcal{L} = \frac{1}{2}\partial_\mu\phi\partial^\mu\phi - \frac{1}{2}m^2\phi^2 - \mathcal{V}(\phi) \tag{2.1}$$

by means of Legendre transformation, the Hamiltonian density may be also obtained, taking the form

$$\mathcal{H} = \frac{1}{2}\dot{\phi}^2 + \frac{1}{2}\nabla\phi^*.\nabla\phi + \mathcal{V}(\phi), \tag{2.2}$$

being the axion potential a periodic function of $\phi(x)$ in such a way that $\mathcal{V}(\phi) = \mathcal{V}(\phi + 2\pi f)$.

In our treatment we are going to account only for field theories with a Z_2 symmetry, so that the relativistic potential is going to be an even function of the scalar field. By the right election of an additive constant, we are able to ensure a minimum of the potential equal zero at $\phi = 0$.

The starting point for the axion self-interactions is the so-called *instanton potential*

$$\mathcal{V}(\phi) = m^2 f^2[1 - \cos(\phi/f)]. \tag{2.3}$$

This relativistic potential was first derived by Peccei and Quinn [24] for the QCD axion in two different ways: keeping only terms that are leading order in Yukawa coupling constants and in the self-interaction coupling constants for the complex scalar field with $U(1)_{PQ}$, or at all orders in the coupling constants by means of the dilute instanton gas approximation. As none of them is fully valid, and there is no way to systematically improve upon them, the instanton potential should be seen, at best, as a model giving just a qualitative picture of axion self-interactions in this momentum regime.

Other options for this potential have been also suggested, as the *chiral potential* [25], but they are also limited approximations.

The power-series expansion of the instanton potential in powers of ϕ^2 will take the form

$$\mathcal{V}(\phi) = m^2 f^2 \sum_{n=2}^{\infty} \frac{\lambda_{2n}}{(2n)!}\left(\frac{\phi^2}{f^2}\right)^n, \tag{2.4}$$

being the coefficients λ_{2n} dimensionless coupling constants.

Notice that f, being positive definite, give us a loop-counting device: if the relation m/f is small, loop diagrams are suppressed by a factor of m^2/f^2 for every loop. This is

the main reason why, in the case of the QCD axion for example, the relativistic axion field theory can be treated as a classical field theory, as this already mentioned factor is roughly 10^{-48} in that case.

The dimensionless coupling constants λ_{2n} for the axion self interactions, defined previously in (2.3), are found to be $\lambda_{2n} = (-1)^{n+1}$. As $\lambda_4 = -1$, the axion pairs self-interactions are attractive.

2.2 Non-relativistic Axion Effective Field Theory

Before considering this new momentum regime below the axion mass m_a, a brief comment is needed concerning the non-relativistic reduction of a real scalar field $\phi(x)$ by means of a complex scalar field $\psi(x)$.

At first sight, one may think that, as the real and imaginary parts of the complex scalar field are in fact two fields, we are describing a different number of degrees of freedom before and after this reduction, what makes no sense.

However, this is not the case. The crucial point to understand why, lies in the fact the relativistic equations of motion for the real scalar field are second order in time derivatives, while for the complex scalar field, the non-relativistic equations of motion are instead first order in time. As it is known, the number of propagating degrees of freedom in the former case is equal to the number of real fields, while in the last case it is equal to half the number of real fields, what makes this real to complex non-relativistic reduction perfectly valid.

Having clarified this point and as a first step, lets consider what will be called the *naive non-relativistic reduction*. In this case, the relation between the real and complex scalar fields is simply

$$\phi(\mathbf{r},t) = \frac{1}{\sqrt{2m_a}}[\psi(\mathbf{r},t)e^{-im_at} + \psi^*(\mathbf{r},t)e^{im_at}], \tag{2.5}$$

where $\psi(\mathbf{r},t)$ is a slowly varying complex scalar field.

Performing this transformation in the original Lagrangian (2.1) and dropping the rapidly oscillating terms, we obtain a Lagrangian density of the form

$$\mathcal{L}_{naive} = \frac{i}{2}(\psi^*\dot{\psi} - \dot{\psi}^*\psi) - \frac{1}{2m_a}\nabla\psi^*.\nabla\psi - \mathcal{V}_{naive}(\psi^*\psi) \tag{2.6}$$

Something similar is done concerning $\mathcal{V}_{naive}(\psi^*\psi)$. Once again, if we drop the terms containing a rapidly oscillating phase factor e^{inmt}, being n a nonzero integer, and also the terms proportional to $\dot{\psi}$ and $\dot{\psi}^*$, the n^{th} term in the power series expansion (2.4) will be

$$\left(\frac{\phi}{f}\right)^{2n} = \frac{(2n)!}{(n!)^2}\left(\frac{\psi^*\psi}{2m_af^2}\right)^n (+ \text{ rapid oscillations}).$$

Considering this the naive potential will take the form

$$\mathcal{V}_{naive}(\psi^*\psi) = m_a^2 f^2 \sum_{n=2}^{\infty} \frac{\lambda_{2n}}{(n!)^2} \left(\frac{\psi^*\psi}{2m_a f^2} \right)^n . \tag{2.7}$$

Here, only the first order term in the expansion (2.7) will lead us to the right coefficient as it will be clearly seen when we compare it with the effective potential obtained using effective field theory matching methods. More specifically, what will be done is to assume the general form of the effective potential in a power-series expansion and each term's coefficient is going to be obtained by matching low-energy $n \to n$ axion scattering amplitudes. With this objective, the procedure exposed in [25] (together with some corrections subsequently introduced in [26]) will be followed. Moreover, we are going to consider other two completely different treatments, leading to valid non-relativistic reductions, which are later shown as equivalent.

The effective Lagrangian density in axion EFT, a non-relativistic effective field theory describing the axion field and its self-interactions at momentum scales smaller than the axion mass m_a, takes the form

$$\mathcal{L}_{eff} = \frac{i}{2}(\psi^*\dot{\psi} - \dot{\psi}^*\psi) - \mathcal{H}_{eff} \tag{2.8}$$

where $\mathcal{H}_{eff}$ depends on ψ^*, ψ and their spatial derivatives. The term explicitly shown in $\mathcal{L}_{eff}$ is the only one containing time derivatives. The effective Lagrangian density presents a global $U(1)$ symmetry in which the field $\psi(x)$ is multiplied by a phase. The invariance under this transformation suggest that every term in $\mathcal{L}_{eff}$ must present equal number of factors of ψ and ψ^*. In this spirit, we will refer to a term with n factors of ψ and n factors of ψ^* as a *n-body term*.

The effective Hamiltonian density in (2.8) is

$$\mathcal{H}_{eff} = \mathcal{T}_{eff} + [\mathcal{V}_{eff} + \mathcal{W}_{eff}] - i[\mathcal{X}_{eff} + \mathcal{Y}_{eff}]. \tag{2.9}$$

In particular all the 1-body terms, with two gradients or more at each term will be contained in the first addend of the Hamiltonian density, generally called *kinetic energy density* $\mathcal{T}_{eff}$. The other four addends are interaction terms which are 2-body or higher, may be separated in two groups, each one with its real and an imaginary part. While the effective potential $\mathcal{V}_{eff} - i\mathcal{X}_{eff}$ is a function of $\psi^*\psi$, the term $\mathcal{W}_{eff} - i\mathcal{Y}_{eff}$ have at least two gradients acting on ψ and ψ^*.

Just by analyzing the kinetic energy density, we have an idea of the limitations of the previous naive reduction. This first term of $\mathcal{H}_{eff}$ is

$$\mathcal{T}_{eff} = \frac{1}{2m_a}\nabla\psi^*.\nabla\psi - \frac{1}{8m_a^3}\nabla^2\psi^*.\nabla^2\psi + \frac{1}{16m_a^5}\nabla(\nabla^2\psi^*).\nabla(\nabla^2\psi) + ... \tag{2.10}$$

As may be easily seen, $\mathcal{L}_{naive}$ contains only the first term in $\mathcal{T}_{eff}$, this is, just the one body term with two gradients, what makes the naive non-relativistic reduction lead to a poor reproduction of the relativistic energy momentum relation $E = \sqrt{m_a^2 + \mathbf{p}^2}$. On the other hand, taking into account that the dots in (2.10) stand for terms with higher number of gradients, the axion EFT Lagrangian density will reproduce the already mentioned relation accurately at higher orders in $\mathbf{p}^2/m_a^2$. In [25], only the first term in the kinetic energy density was included, being corrected later in [26].

Lets focus now on the rest of $\mathcal{H}_{eff}$. In particular, for the derivation of the real part of the effective potential, EFT matching methods are going to be used. Our first step will be to assume that low-energy axions could be described by means of the the Lagrangian for the relativistic real scalar field $\phi(x)$ (2.1) and by the effective Lagrangian for the non-relativistic complex field $\psi(x)$ on axion EFT (2.8), in an precise and equivalent manner.

More specifically, $\mathcal{V}_{eff}$ will be also expressed as a power-series expansion

$$\mathcal{V}_{eff}(\psi^*\psi) = m_a^2 f^2 \sum_{j=2}^{\infty} \frac{v_j}{(j!)^2} \left(\frac{\psi^*\psi}{2m_a f^2} \right)^j , \tag{2.11}$$

and what will be determined by matching low-energy scattering amplitudes in the relativistic theory and in axion EFT will the coefficient of each term.

In this process, we consider only tree diagrams. This assumption is in principle well justified for specific case as the QCD axion. For it, loop diagrams are suppressed in relativistic theory, being only necessary to match the contributions to low-energy scattering amplitudes from tree-level diagrams in the relativistic theory with tree-level diagrams in axions EFT. In the situations in which this assumptions is not justified, the loop diagrams should be also considered in the calculations of the coefficients presented below.

Some clarifications are also needed concerning the expansion (2.11). First of all, stress that an additive constant have been included in $\mathcal{V}_{eff}$ in such a way that the potential presents a minimum of zero at $\psi^*\psi = 0$. Also say that, in [25], the mass-energy term $m_a\psi^*\psi$ was included in the effective potential. With this, the equations of motion include a term with the form $\psi(\mathbf{r}, t)e^{im_a t}$, having large frequencies of order m_a. Nevertheless, in EFT seems more appropriate to eliminate the scale m_a, in such a way that $\psi(\mathbf{r}, t)$ presents only frequencies much smaller than m_a.

Now, in order to give a more clear vision of the already mentioned matching process, we are going to consider the calculation of the three first coefficients, this is v_2,v_3 and v_4. However, nothing stop us to continue to higher v_n.

Concerning the very first coefficient, the only contribution at tree-level comes from the $2 \to 2$ vertex diagram. While the Feynman rule for that vertex in the relativistic theory is $-i\lambda_4 m_a^2/f^2$ in axion EFT will be $-i(4m_a^2)v_2/4f^2$, where squared axion mass factor arises to keep the standard relativistic normalization of single-particles states in

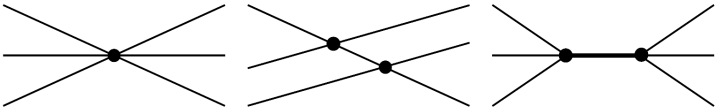

Figure 2.1: The tree-level diagrams for low-energy $3 \to 3$ scattering in the relativistic axion theory. The thicker line appearing in the last diagram represent virtual axion with ~ 3m. Figure obtained from [25].

the scattering amplitude, multiplying by four factors of $\sqrt{2m_a}$. Matching the scattering amplitudes, we obtain

$$v_2 = \lambda_4. \tag{2.12}$$

Slightly more complicated are the next two coefficients. For v_3 we have to consider obviously the $3 \to 3$ axion scattering amplitudes. The tree-level diagrams for $3 \to 3$ axion vertexes are shown in Figure 2.1. The first diagram is simply the $3 \to 3$ vertex. In the second one, a virtual axion line connects the two $2 \to 2$ vertices.

While the former two diagrams contribute to the axion EFT, the last one do not, as the virtual axion line connecting both vertexes is in fact relativistic, with $\sim 3m_a$. The third diagram has 3 axions scattering into a single virtual axion and then back into three axions. The matching procedure, as previously done for the previous v_2, lead us to

$$v_3 = \lambda_6 - \frac{17}{8}\lambda_4^2. \tag{2.13}$$

At last, v_4 is determined by matching the $4 \to 4$ scattering from the tree-level diagrams in Figure 2.2. From these 11 diagrams only 6 of them contribute to axion effective field theory, for the already mentioned reason. The value for v_4 will be

$$v_4 = \lambda_8 - 11\lambda_4\lambda_6 + \frac{125}{8}\lambda_4^3. \tag{2.14}$$

As said before, simply by comparing these coefficients with obtained for the naive potential, we see once again the limitations of that non-relativistic reduction, as it leads to the correct result just for the first coefficient v_2 as may be seen in (2.12). The other two, and presumably any other at higher order, are not correctly calculated as (2.13) and (2.14) suggest.

The final form for $\mathcal{V}_{eff}$ is then

$$\begin{aligned}\mathcal{V}_{eff}(\psi^*\psi) = \frac{\lambda_4}{16\, m_a f^2}(\psi^*\psi)^2 + \left[\lambda_6 - \frac{17}{8}\lambda_4^2\right]\left(\frac{(\psi^*\psi)^3}{288\, m_a f^4}\right) + \\ + \left[\lambda_8 - 11\lambda_4\lambda_6 + \frac{125}{8}\lambda_4^3\right]\left(\frac{(\psi^*\psi)^4}{9216\, m_a^2 f^6}\right) + \ \dots\ ,\end{aligned} \tag{2.15}$$

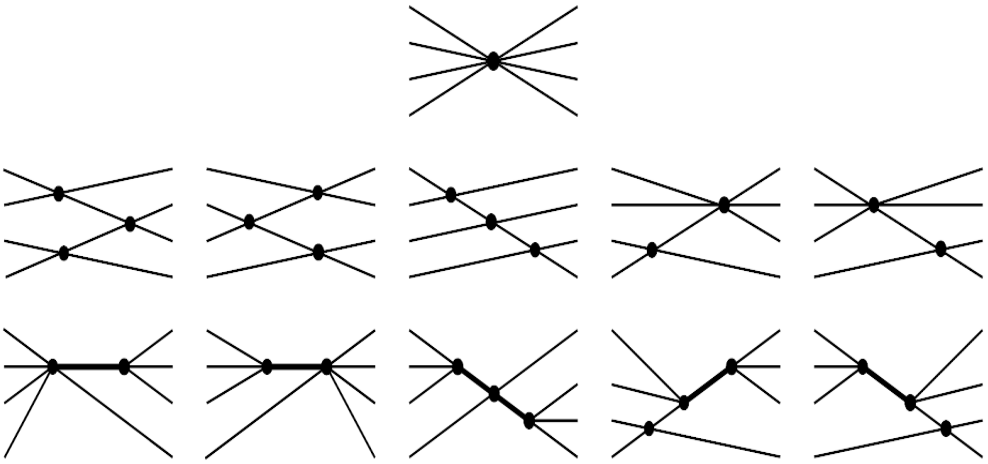

Figure 2.2: The tree-level diagrams for low-energy $4 \to 4$ scattering in the relativistic axion theory, where only the first 6 diagrams are also diagrams in axion EFT. The thicker line appearing in the last 5 diagrams represent virtual axion with ~ 3m. Figure obtained from [25].

where the dots stand for higher order terms.

Before conclude this section, a brief comment concerning the imaginary part of the interaction terms is necessary. The imaginary terms $i\mathcal{X}_{eff}$ and $i\mathcal{Y}_{eff}$ are the only two non-Hermitian addends (being in fact anti-Hermitian) of the Hamiltonian density $\mathcal{H}_{eff}$. In their absence, a global $U(1)$ symmetry will be present and the particle number

$$N = \int d^3r \; \psi^*\psi, \tag{2.16}$$

should be conserved.

Because of this, the rate of decrease in the particle number will be directly linked with them, in such a way that

$$\frac{d}{dt}N = -2 \int d^3r \; [\mathcal{X}'_{eff}(\psi^*\psi)\psi^*\psi + ...\,], \tag{2.17}$$

being $\mathcal{X}'_{eff}$ the derivative of $\mathcal{X}_{eff}$ with respect to $\psi^*\psi$ and where the dots stand for additional terms linked with the interaction terms in $\mathcal{Y}_{eff}$, with gradients of ψ and ψ^*.

2.3 Improved effective potentials

In general, if $\psi^*\psi$ is much less than $m_a f^2$, truncate the power-series expansion defining the effective potential $\mathcal{V}_{eff}$ (2.11) at a certain power (as for instance keeping only the

terms explicitly shown in (2.15)) it is, considering enough terms, a good approximation.

On the other hand when this is not the case, we need to keep terms of each power of $\psi^*\psi$. A first approximation to the effective potential for the axion EFT that includes terms of all orders in $\psi^*\psi$ is calculated from the previous naive non-relativistic reduction.

In [25], Braaten et al. denote the naive effective potential (2.7) as $\mathcal{V}^{(0)}_{eff}(\psi^*\psi)$. This suggest that it will be taken as the first of a series of improved effective potentials.

The crucial point to understand this identification lies in the fact that the naive effective potential may be obtained by approximating the coefficients in the power series (2.11) for the effective potential $\mathcal{V}_{eff}$ by $v^{(0)}_n \equiv \lambda_{2n}$. In EFT, this is equivalent to matching the contributions to the $n \to n$ scattering amplitudes, at all n, only for diagrams with no virtual propagators. These diagrams are the $2n$ axion vertex in the relativistic theory and the $n \to n$ vertex in axion EFT. In the cases of $n = 3$ and $n = 4$ they correspond to the first diagrams in Figure 2.1 and Figure 2.2 respectively.

So, matching the $n \to n$ scattering amplitude for all n, considering diagrams with at most k virtual propagators, we are able to define a series of effective potentials $\mathcal{V}^{(k)}_{eff}$, being $k = 0, 1, 2, ...$ As said before, the non-relativistic reduction potential or naive potential $\mathcal{V}^{(0)}_{eff}$ will be the first term of this series, with $k = 0$, and the rest of the potentials $\mathcal{V}^{(k)}_{eff}$ with $k \geq 1$, are the so called *improved effective potentials*, defined as

$$\mathcal{V}^{(k)}_{eff}(\psi^*\psi) = m_a^2 f^2 \sum_{n=2}^{\infty} \frac{v^{(k)}_n}{(n!)^2} \left(\frac{\psi^*\psi}{2m_a f^2} \right)^n . \tag{2.18}$$

In general, the coefficients $v^{(k)}_n$ agree with the exact coefficients v_n for $n = 2, ..., k + 2$. Considering this, as k increases, the different $\mathcal{V}^{(k)}_{eff}(\psi^*\psi)$ will be more accurate at large $\psi^*\psi$, as bigger classes of diagrams are summed. At last, we expect the sequence $\mathcal{V}^{(k)}_{eff}(\psi^*\psi)$ to converge to $\mathcal{V}_{eff}$ as $k \to \infty$, as all diagrams are included in this limit.

See [25], for the details concerning the explicit calculation of the first improved effective potential $\mathcal{V}^{(1)}_{eff}(\psi^*\psi)$.

2.4 Other Classical Non-Relativistic EFT

Even though the derivation we have just presented is perfectly complete and correct, other diverse classical non-relativistic effective field theories (CNREFT) have been suggested, being their equivalence shown explicitly in [26]. In this section, we are going to briefly review the main characteristics and the effective Lagrangian of two of them: the non-local field transformation of Namjoo, Guth and Kaiser [27] and the Mukaida, Takimoto and Yamada CNREFT [19].

2.4.1 Non-Local Field Transformation

The main innovation introduced in [27] was an exact but non-local transformation between a relativistic real valued scalar field $\phi(x)$ and a complex field $\psi(x)$. In particular, they consider a relativistic scalar field of mass m and a $\lambda\phi^4$ self-interaction described by

$$\mathcal{L} = \frac{1}{2}\partial_\mu\phi\partial^\mu\phi - \frac{1}{2}m^2\phi^2 - \frac{\lambda}{4!}\phi^4, \tag{2.19}$$

with canonical momentum field $\pi(x) = \dot{\phi}(x)$.

By contrast the Lagrangian density for a free non-relativistic field will be

$$\mathcal{L} = \frac{i}{2}(\psi^*\dot{\psi} - \dot{\psi}^*\psi) - \frac{1}{2m}\nabla\psi^*.\nabla\psi, \tag{2.20}$$

with an explicit global $U(1)$ symmetry, linked with the particle number conservation, as expected. Here, $\psi(x)$ and $\psi^*(x)$ obey the standard Poisson bracket relation, what means that the standard commutation relations, when quantized, will be fulfilled.

As a starting point in the process leading us to this new non-local reduction, lets consider once again the naive non-relativistic reduction (2.5). Even though, is not usually written explicitly, the uniqueness of $\psi(\mathbf{r}, t)$ demands a similar relation concerning the canonical momentum field,

$$\pi(\mathbf{r}, t) = -i\sqrt{\frac{m}{2}}[\psi(\mathbf{r}, t)e^{-imt} - \psi^*(\mathbf{r}, t)e^{imt}]. \tag{2.21}$$

The systematical way of obtaining the relativistic corrections to the non-relativistic theory suggested by Namjoo et al. consist in a similar non-relativistic reduction with a non-local field operator, this is

$$\phi(\mathbf{r}, t) = \frac{1}{\sqrt{2m}}\mathcal{P}^{-1/2}[\psi(\mathbf{r}, t)e^{-imt} + \psi^*(\mathbf{r}, t)e^{imt}] \tag{2.22}$$

$$\pi(\mathbf{r}, t) = -i\sqrt{\frac{m}{2}}\mathcal{P}^{1/2}[\psi(\mathbf{r}, t)e^{-imt} - \psi^*(\mathbf{r}, t)e^{imt}], \tag{2.23}$$

where we have that

$$\mathcal{P} \equiv \sqrt{1 - \frac{\nabla^2}{m^2}}, \tag{2.24}$$

being $m\mathcal{P}$ the total energy of a free relativistic particle.

The crucial fact which needs to be understood at this stage is that, in the non-relativistic limit, the new fields $\psi(x)$ and $\psi^*(x)$ will be well behaved despite the non-local operator, as in this limit the operator $\mathcal{P}$ could be expanded in powers of ∇^2/m^2. Notice also that, considering just the leading order in this expansion of the non-local operator $\mathcal{P}$, we recover the naive non-relativistic reduction.

Once this has been clarified, it is straightforward to obtain the equation of motion for $\psi(\mathbf{r},t)$, this is

$$i\dot{\psi} = m(\mathcal{P}-1) + \frac{\lambda e^{imt}}{24m^2}\mathcal{P}^{-1/2}[e^{-imt}\mathcal{P}^{-1/2}\psi + e^{imt}\mathcal{P}^{-1/2}\psi^*]^3, \tag{2.25}$$

and the Lagrangian density for this non-local formulation will be

$$\mathcal{L} = \frac{i}{2}(\psi^*\dot{\psi} - \dot{\psi}^*\psi) - m\psi^*(\mathcal{P}-1)\psi - \frac{\lambda}{96m^2}[e^{-imt}\mathcal{P}^{-1/2}\psi + e^{imt}\mathcal{P}^{-1/2}\psi^*]^4. \tag{2.26}$$

Now, lets try to obtain the description for this model in the non-relativistic regime. In general, the objective is to take the non-relativistic limit but incorporating relativistic corrections systematically. So, apart from expanding the non-local operator $\mathcal{P}$ in powers of ∇^2/m^2, it is necessary to account for the effect of fast-oscillating terms on the behavior of the slowly varying field.

The idea introduced in [27] is to construct a perturvative approach, which considers the contribution to the time evolution of the slowly varying portion of the field $\psi(x)$ of the fast-oscillating terms.

The final form of the resulting effective Lagrangian will be

$$\begin{aligned}\mathcal{L}_{eff} = \frac{i}{2}(\psi_s^*\dot{\psi}_s - \dot{\psi_s}^*\psi_s) - \frac{1}{2m}\nabla\psi_s^*.\nabla\psi_s - \frac{\lambda}{16m^2}|\psi_s|^4 + \\ + \frac{1}{8m^3}\nabla^2\psi_s^*.\nabla^2\psi_s - \frac{\lambda}{32m^4}|\psi_s|^2(\psi_s\nabla^2\psi_s^* + \psi_s^*\nabla^2\psi_s) + \frac{17\lambda^2}{2304m^5}|\psi_s|^6,\end{aligned} \tag{2.27}$$

where ψ_s is the $\nu = 0$ mode in the expansion

$$\psi(\mathbf{r},t) = \sum_{\nu=-\infty}^{\infty}\psi_\nu(\mathbf{r},t)e^{i\nu mt}, \tag{2.28}$$

being each $\psi_\nu(\mathbf{r},t)$ slowly varying on a time scale of the order m^{-1}, and

$$\psi_{\nu=0}(\mathbf{r},t) \equiv \psi_s(\mathbf{r},t). \tag{2.29}$$

Notice that the effective Lagrangian for $\psi_s(x)$ in (2.27) presents interaction terms that lead us both to $2 \to 2$ and $3 \to 3$ scatterings. Also, including more terms of the iterative expansion (2.28) for $\psi_\nu(x)$ with $\nu \neq 0$ would lead us to operators in $\mathcal{L}_{eff}$ for each $n \to n$ for $n > 1$.

The final effective Lagrangian obeys a global $U(1)$ symmetry and this characteristic holds at all orders in the NREFT. Processes as $4 \to 2$ scattering, in which the two outgoing particles are relativistic, with energies $E \gg m$, lie beyond the validity of $\mathcal{L}_{eff}$.

At last, in [27], an application of this treatment for case of the QCD axions in the non-relativistic limit is presented, compared first with the one reviewed preivously [25] and also, in Appendix C, with a different treatment introduced in [19] that we are going to review in the next subsection.

2.4.2 MTY Effective Theory

Mukaida et al. [19] consider instead the following relativistic real scalar field theory

$$\mathcal{L} = \frac{1}{2}\partial_\mu\phi\partial^\mu\phi - \frac{1}{2}m^2\phi^2 - \mathcal{V}_{int}(\phi), \tag{2.30}$$

being $\phi(x)$ the real scalar field with mass m and $\mathcal{V}_{int}$ the interaction term.

Their method consists in the derivation of an effective field theory which describes the non-relativistic behaviour of $\phi(x)$ by integrating out the relativistic modes from the Lagrangian.

For this propose, the scalar field is separated in two parts, one of them completely non-relativistic and the rest

$$\phi(\mathbf{x}) = \phi_{nr}(\mathbf{x}) + \delta\phi(\mathbf{x}), \tag{2.31}$$

being

$$\phi_{nr}(\mathbf{x}) \equiv \int_{K\in nr} dK\ e^{-iKx}\phi(K), \tag{2.32}$$

$$\delta\phi(\mathbf{x}) \equiv \int_{K\in\overline{nr}} dK\ e^{-iKx}\phi(K). \tag{2.33}$$

with $K^\mu = (k^0, k)$. Here, nr indicates the region close to the on-shell poles of non-relativistic excitations, *i.e.*, $nr \equiv \{(k_0, k|\pm k_0 \sim m + \mathcal{O}(mv^2), k \sim \mathcal{O}(mv)\}$ with $|v| \ll 1$. $\overline{nr}$ is defined as the complementary set.

$\phi(K)$ is the Fourier coefficient of the real scalar field, which satisfies $\phi(K) = \phi^*(-K)$. The non-relativistic part of the scalar filed $\phi_{nr}(\mathbf{x})$ is expressed as a function of the a complex scalar field $\psi(\mathbf{x})$ by means of the naive non-relativistic reduction (2.5).

Concerning the interaction potential, it will present a minimum at $\phi = 0$ with the usual expansion in even powers previously presented. The case with an extra cubic term is also treated in the original paper.

Once the complex field has been properly re-scaled in such a way that the coefficient of the $\nabla\psi^*.\nabla\psi$ term is the usual $-1/2m$, the real part of the *MTY effective Lagrangian* will be

$$Re[\mathcal{L}_{MTY}] = \frac{i}{2}(\psi^*\dot{\psi} - \dot{\psi}^*\psi) + \frac{1}{2m}\dot{\psi}^*\dot{\psi} - \frac{1}{2m}\nabla\psi^*.\nabla\psi - V_{MTY} - W_{MTY}, \tag{2.34}$$

where V_{MTY} is a function of $\psi^*\psi$ and W_{MTY} consist of terms with gradients or time derivatives of $\psi(x)$ and $\psi^*(x)$. Both of them are explicitly shown in [26].

Even though the form of $\mathcal{L}_{MTY}$ seems to the differ at first sight from $\mathcal{L}_{eff}$ (2.8), as the former contains, among other things, a term with two time derivatives, these two effective Lagrangian are shown equivalent in Section V of [26] as they lead to the same T-matrix elements. The discrepancy is shown to be simply due to a different definition of the complex field $\psi(x)$ and the redefinition needed to obtain the same effective Lagrangian, following any of the two paths, is also given.

Chapter 3

Scalar Stars

Now that we have clarified the main points concerning the non-relativistic reduction and the axion EFT, we are ready for the analysis of the meta-stability of the axion stars. It will be performed by means of the non-relativistic effective field theory, well justified as said before, while we work in the momentum regime below the axion mass.

In this chapter we will first obtain the so called *Schrodinger-Newton system of equations*, crucial for the study of the stability regimes of the scalar and axion stars. After that we are going to perform our analysis considering diverse self-interaction potentials, from the simplest cases to others containing higher order terms.

3.1 Schrodinger-Newton equations

For the moment, we are going to consider the naive non-relativistic reduction (2.5). Its use is justified by the fact that, for now, we are going to take only the leading non-linear term in potential (2.7). As previously calculated in (2.12), the first coefficient obtained by means of this naive relation coincide with the exact one, obtained by means of axion EFT.

The Lagrangian describing the dynamics of the axion is very similar to (2.6) but considering the weak field Newtonian metric $g_{00} = 1 + 2\varphi_N(\psi^*, \psi)$, being φ_N the Newtonian potential, to account for the gravitational effects

$$\mathcal{L}_{naive} = \frac{i}{2}(\psi^*\dot{\psi} - \dot{\psi}^*\psi) - \frac{1}{2m_a}\nabla\psi^*.\nabla\psi - \mathcal{V}_{naive}(\psi^*\psi) - m_a\psi^*\psi\ \varphi_N(\psi^*, \psi). \tag{3.1}$$

Here, axion self-interactions will be generated in the relativistic regime by the instanton potential (2.3), and then the power-series expansion of the cosine leads us to $\lambda_4 = -1$. Therefore the leading non-linear term in the non-relativistic potential is

$$V_{naive}(\psi, \psi^*) = -\frac{\psi^{*2}\psi^2}{16f^2}. \tag{3.2}$$

By performing a Legendre transformation, the total *naive Hamiltonian* can be expressed by the sum of three terms

$$H_{naive} = H_{kin} + H_{int} + H_{grav}, \tag{3.3}$$

where

$$H_{kin} \equiv \frac{1}{2m_a} \int d^3x \; \nabla\psi^*.\nabla\psi, \tag{3.4}$$

$$H_{int} \equiv \int d^3x \; V_{naive}(\psi, \psi^*), \tag{3.5}$$

$$H_{grav} \equiv -\frac{Gm_a^2}{2} \int d^3x \int d^3x' \; \frac{\psi^*(\mathbf{x})\psi^*(\mathbf{x}')\psi(\mathbf{x})\psi(\mathbf{x}')}{|\mathbf{x}-\mathbf{x}'|}, \tag{3.6}$$

where G is the gravitational constant. H_{kin}, H_{int} and H_{grav} represent the kinetic energy, the self-interaction energy and the gravitational energy, respectively and an overall rest mass energy term has been dropped, as it leads merely to a constant.

The full equation of motion will be

$$i\dot{\psi} = -\frac{\nabla^2\psi}{2m_a} - Gm_a^2\psi \int d^3x' \; \frac{\psi^*(\mathbf{x}')\psi(\mathbf{x}')}{|\mathbf{x}-\mathbf{x}'|} - \frac{\partial}{\partial\psi^*}\left(\frac{\psi^{*2}\psi^2}{16f^2}\right). \tag{3.7}$$

In order to describe the full non-linear evolution of the axionic field, with the added assumption of spherical symmetry, we solve the system of coupled equations formed by the previous equation of motion for the axion field (3.7) together with the Poisson equation for the Newtonian potential, the so-called Schrodinger-Newton system of equations with the form

$$i\frac{\partial\tilde{\psi}}{\partial\tilde{t}} = -\frac{1}{2\tilde{r}}\frac{\partial^2}{\partial\tilde{r}^2}(\tilde{r}\tilde{\psi}) + \tilde{\varphi}_N\tilde{\psi} - \frac{1}{8}|\tilde{\psi}|^2\tilde{\psi} \tag{3.8}$$

$$\frac{1}{\tilde{r}}\frac{\partial^2}{\partial\tilde{r}^2}(\tilde{r}\tilde{\varphi}_N) = 4\pi|\tilde{\psi}|^2 \tag{3.9}$$

where $\tilde{\psi}(\tilde{r},\tilde{t})$ represents the axion field, $\tilde{\varphi}_N(\tilde{r},\tilde{t})$ the Newtonian potential and $\tilde{r}$ and $\tilde{t}$ are the radial and time variables. All the variables have been rendered dimensionless by means of suitable rescalings.

In Section 4 of [16], this system of coupled differential equations is solved numerically using the *Crank-Nicholson* method.

In our case, we are going to assume that the ground state configuration takes the form

$$\psi(r,t) = \psi(r)e^{-i\mu t} \tag{3.10}$$

being μ the chemical potential. Here the radial and time dependence have been separated, being the first concentrated in $\psi(r)$, while the time dependence lies in the exponential.

The assumption of spherical symmetry is both driven by simplicity and by the fact that such configurations are the lowest energy states of the system. As in the well known case of the Hydrogen atom, the ground state is in fact spherically symmetric while the non-spherically symmetric eigenstates, with Y_{lm} and $l > 0$, have higher energy. Also, as this discussion concerns a scalar field, there is no mechanism to spontaneously break the spherical symmetry of the ground state, as could occur for a vector field. As we will be mainly focused in this ground state with a fixed N, the spherical symmetry will be guaranteed.

With these assumptions we now have to solve the stationary version of this system of coupled differential equations

$$\tilde{E}\tilde{\psi} = -\frac{1}{2\tilde{r}}\frac{\partial^2}{\partial\tilde{r}^2}(\tilde{r}\tilde{\psi}) + \tilde{\varphi}_N\tilde{\psi} - \frac{1}{8}|\tilde{\psi}|^2\tilde{\psi} \tag{3.11}$$

$$\frac{1}{\tilde{r}}\frac{\partial^2}{\partial\tilde{r}^2}(\tilde{r}\tilde{\varphi}_N) = 4\pi|\tilde{\psi}|^2 \tag{3.12}$$

being $\tilde{E}$ the dimensionless energy eigenvalue.

To solve this system of non-linear coupled differential equations, we are going to use the procedure introduced by Moroz et al. in [28]. In the next subsection, we will review the details of this method and its application to a simpler case of the Schrodinger-Newton equations, that is, the same system of equations but with negligible self-interactions, eliminating the last term in (3.11). Once these details are clear, this procedure will be used to obtain the axion field solution of the system of equations (3.11) and (3.12), paying special attention to the difference between both cases. After that, by means of diverse ansatzs for the radial part of the solution, we are going to find an analytical version of the Hamiltonian, which will allow us to study the physical stability of the solutions. At last, we will study the phase diagram, where the stability regimes are shown. This full analysis will be repeated in the case with a single self-interaction term of equations (3.11) and (3.12), but also considering more complicated self-interactions potentials.

3.2 Negligible Self-interactions

Although the Schrodinger-Newton equations emerge in [28] in the context of a totally different problem, the procedure proposed will be fully applicable to our case. In particular, this system of equations is introduced in the context of *quantum state reduction*. The original shape of this pair of partial differential equations (equation (1a) and (1b) in the already mentioned paper) is

$$E\psi = -\frac{\hbar^2}{2m}\nabla^2\psi + \varphi_N\psi, \tag{3.13}$$

$$\nabla^2\varphi_N = 4\pi\gamma|\psi|^2, \tag{3.14}$$

where the notation has been adapted to coincide with the previous one. Here, $\gamma = Gm^2$ and being $\hbar$ the reduced Plank constant.

As a first step, we are going to redefine the two variables as

$$\psi(\mathbf{x}) = \alpha S(\mathbf{x}), \tag{3.15}$$

$$E - \varphi_N(\mathbf{x}) = \beta V(\mathbf{x}), \tag{3.16}$$

where α and β are constants defined as

$$\alpha \equiv \left[\frac{\hbar^2}{8\pi G^3}\right]^{1/2}, \tag{3.17}$$

$$\beta \equiv \frac{\hbar^2}{2m}. \tag{3.18}$$

Assuming also, without loss of generality, that $\psi(\mathbf{x})$ is real, we find that the Schrodinger-Newton system can be recast as

$$\nabla^2 S = -SV, \tag{3.19}$$

$$\nabla^2 V = -S^2. \tag{3.20}$$

Note that there is a scale invariance in the system of equations (3.19) and (3.20) under the transformation

$$(S, V, r) \longrightarrow (\lambda^2 S,\ \lambda^2 V,\ \lambda^{-1} r), \tag{3.21}$$

λ being real.

For now on, we are going to limit ourselves to the spherically symmetric case, in such a way that S and V will be functions of r only. This leads us to

$$(rS)'' = -rSV, \tag{3.22}$$

$$(rV)'' = -rS^2, \tag{3.23}$$

where the prime denotes, from now on, differentiation with respect to r. This will be the form of the Schrodinger-Newton equations that are going to be analyzed, with the boundary conditions requiring a well defined Laplacian at the origin $r = 0$, what is translated into vanishing $S'(r)$ and $V'(r)$ there.

Before going on with the numerical procedure itself, we will consider some analytical results which could help us to better understand this system and its solutions.

At first sight the system composed by equations (3.22) and (3.23) will present three different solutions from a pure analytical point of view. The first one is the trivial solution $S = 0$ and $V =$ constant, together with two extra solutions, namely $(S, V) = (\pm 2r^{-2}, -2r^{-2})$. Nevertheless, these two last solutions are unbounded at $r = 0$. Therefore they will not be taken into account as they do not meet the well defined Laplacian at the origin criterion previously introduced.

If the initial values are expressed as $S_0 = S(0)$ and $V_0 = V(0)$, integrating twice the system of coupled differential equations (3.22) and (3.23), we obtain its equivalent system of integral equations

$$S(r) = S_0 - \int_0^r x[1 - \frac{x}{r}]S(x)V(x)dx, \tag{3.24}$$

$$V(r) = V_0 - \int_0^r x[1 - \frac{x}{r}]S^2(x)dx, \tag{3.25}$$

The uniqueness of the solutions will be ensured by means of a modified version of the Picard's theorem (see [29]), given the initial values S_0 and V_0. So for a particular initial conditions, solutions will exist and be unique, at least for an interval $[0, a)$ in r, where a depends upon both S_0 and V_0.

The rescaling freedom in (3.21) will allow us to shorten the range of possible values of S_0 and V_0 without any lost of generality. The first discarded value will be $S_0 = 0$, as for it the uniqueness of solutions will lead us to the trivial solution $S(r) = 0$ and $V(r) =$ constant. We are also able to fix $S_0 = 1$, finding all the range of solutions for the system varying V_0 or vice versa, reducing the dependence to just V_0 or S_0. In particular, our choice will be to fix $V_0 = 1$ and find the diverse solutions by changing the value of S_0. Finally, considering the scale invariance of the system will be able to consider only negative or positive values of S_0 as it is easy to replace S by $-S$ if necessary. In what follows we make the choice of taking only $S_0 > 0$.

Another relevant analytical property, lies in the fact that $V(r)$ decrease monotonically, as its derivative suggests, obtained by differentiating once (3.25)

$$V^{'}(r) = -\frac{1}{r^2}\int_0^r x^2 S^2(x)dx. \tag{3.26}$$

If we fix $S_0 = 1$, the previous equation shows a slightly different behaviour for positive or negative values of V_0. In the case with $V_0 \leq 0$, it may be shown that $S(r) \to \infty$ while $V(r) \to -\infty$. But for $V_0 > 0$ we have instead an initially positive value of $V(r)$, which sooner or later turns into negative, according to (3.26).

Additionally, we will find also a different general behaviour of $rS(r)$, deduced from (3.22) and (3.23), depending on the sign of the potential $V(r)$. While it will be oscillatory for $V(r) > 0$, an exponential dependence is found if $V(r) < 0$, containing a mixture of growing and decaying terms. This tells us that divergences to both plus or minus infinity are possible. Also, together with the fact, deduced from (3.25), that $V(r)$ diverges to $-\infty$ leads us to expect unbounded states, diverging at finite values of r. Our only chance to avoid these unbounded solutions is to have only exponentially decaying terms in $rS(r)$.

The numerical integrations described below will tell us that this can be realized for a discrete set of values V_0/S_0, the so-called *bound states*. For them, $rS(r)$ decays exponentially so that the wave functions are square-integrable and $V(\infty)$ remains finite

by (3.25). Notice due to the fact that these bound states appear for certain values of the ratio V_0/S_0, we are able to fix one of them equal one and vary the other without lost of generality.

The fact that $S(r)$ and $V(r)$ are finite at $r = 0$ together with the condition of a well defined Laplacian at the origin previously introduced, allow us to expand in power-series both of them about $r = 0$

$$S = S_0 - \frac{1}{6}S_0 r^2 + \frac{1}{120}S_0(S_0^2 + 1)r^4 + ... \,, \tag{3.27}$$

$$V = 1 - \frac{1}{6}S_0^2 r^2 + \frac{1}{60}S_0^2 r^4 + ... \,. \tag{3.28}$$

Close to $r = 0$, the solution only depends on S_0 as expected. Different numerical studies have verified the accuracy of this power-series expansion.

What arises from the numerical integration is an infinite set of discrete *unstable bound states*, which seems to accumulate at $S = 0$. By unstable it is understood that an infinite precision in the value of S_0 is required to ensure that the solution do not diverge as r grows. Taking this into account, the more precisely determined our value of S_0 is, the later in r will our solution diverge. Other crucial property of these bound states is that each of them marks the transition form a solution with $(S, V) \to (+\infty, -\infty)$ to another with $(S, V) \to (-\infty, -\infty)$. In order to simplify our notation, we will refer to the first kind as $(+, -)$ states/solutions, while the second ones will be $(-, -)$ states/solutions.

It is crucial to distinguish the stability mentioned here, purely mathematical, from the previously discussed physical (meta-)stability of the axion stars, which is instead completely related with their evolution in time. While all bound state solutions are mathematically unstable in the former sense, from the physical stability point of view, we are going to find both kind of solutions (stable and unstable) in the next sections. From now on, when we talk about stable or unstable solutions, we will be referring to the mentioned physical stability.

So, going back and applying an *order four Runge-Kutta method* to solve numerically the system of coupled differential equations (3.22) and (3.23), as it is done in [28], for $S_0 > 1.09$ we find that $S(r)$ blow up to $+\infty$ at a finite value of r and it does not present any zero. On the other hand for $S_0 < 1.08$ at certain finite value of r, we find a $(-, -)$ solution. This allows us to interpret that we have a bound state in the interval $S_0 = [1.08, 1.09]$, for which $S(r)$ do not diverge, but an infinite precision in S_0 is necessary to reach it. Now, we move on to the next decimal. As for $S_0 > 1.089$ the solution is $(+, -)$, while for $S_0 < 1.088$ it is $(-, -)$, the interval where the bound state is placed is reduced to $S_0 = [1.088, 1.089]$. This process continues iteratively up to the desired precision, always with a fixed $V_0 = 1$. In Figure 3.1 we clearly see what has been previously suggested, that is, a higher accuracy in S_0 is related with the divergence appearing at a bigger value of r, simply by comparing the two $(-, -)$ solutions, represented by blue lines. In Figure 3.2, a representation of $V(r)$, obtained with high

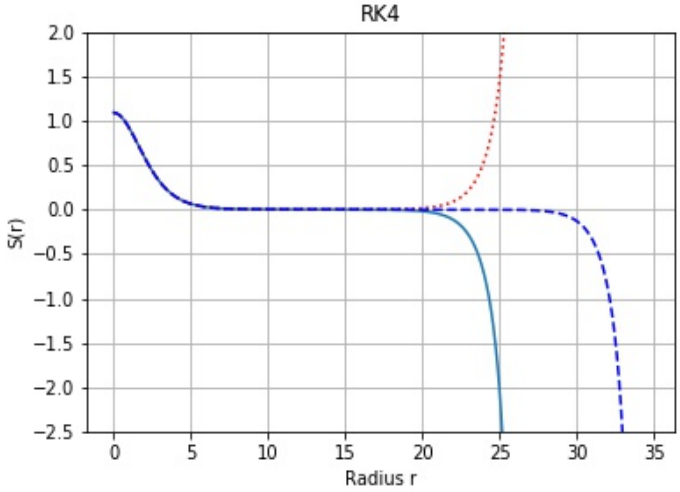

Figure 3.1: The red dotted line represents the first bound-state wavefunction with $S_0 = 1.0886472$, while the solid blue line stands for the first bound-state wavefunction with $S_0 = 1.0886471$. The solution with the dashed blue line has instead a $S_0 = 1.0886471184$. All of them have been obtained using the Runge-Kutta method, with $V_0 = 1$ for all of them.

	Moroz et al [28]	RK4	Euler
$n = 0$	1.0886370794	1.0886471184	1.0890934531
$n = 1$	0.8264742841	0.8264612205	0.8261073336

Table 3.1: S_0 values obtained using the order four Runge-Kutta method (RK4) and the Euler method, up to $\mathcal{O}(10^{-10})$, for the first bound state ($n = 0$) or the second bound state ($n = 1$) compared with the one obtained in the original paper [28], with $V_0 = 1$.

precision in S_0, is shown. We see the expected monotonically decreasing behaviour until the divergence takes place.

Even though is not something relevant for our discussion, this process may be extended to solutions with higher number of zeros. For instance, if in the interval of S_0 the upper end has a single zero before diverging to minus infinity, while the lower has two zeros before going to plus infinity, we talk about the *second bound-state*. An example is shown in Figure 3.3.

Apart from the already mentioned order four Runge-Kutta method, we have also calculated the first bound state by means of a simple *Euler method*, see Figure 3.4, and the different values obtained for S_0 with equal precision have been compared in Table 3.1.

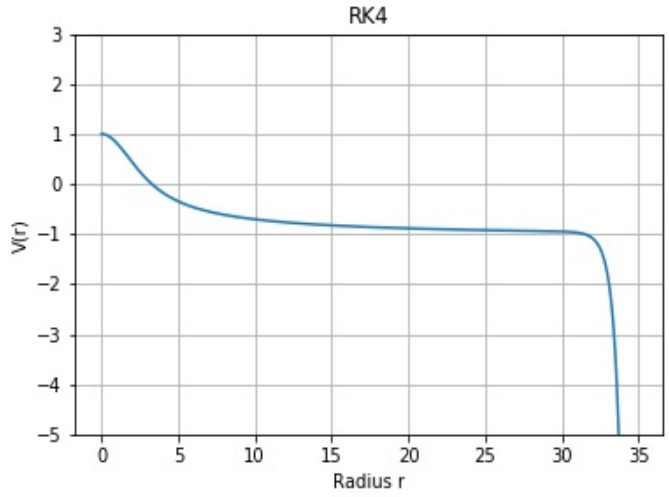

Figure 3.2: Newtonian potential $V(r)$ with $S_0 = 1.0886471184$, being $V_0 = 1$, obtained using the Runge-Kutta method.

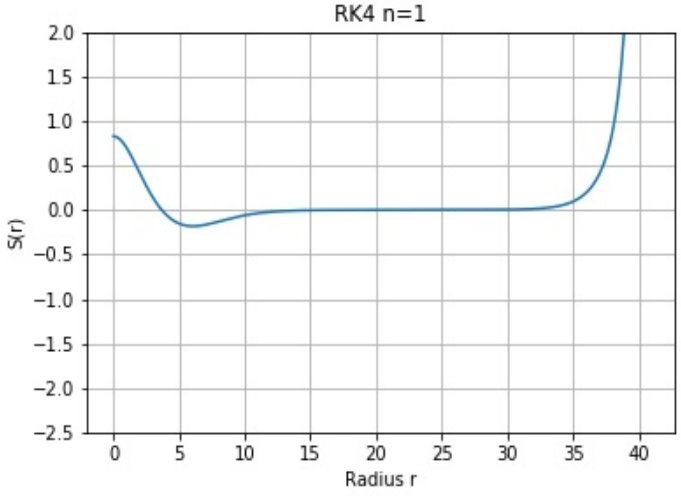

Figure 3.3: Second bound-state wavefunction with $S_0 = 0.8264612205$, obtained using the Runge-Kutta method, with $V_0 = 1$.

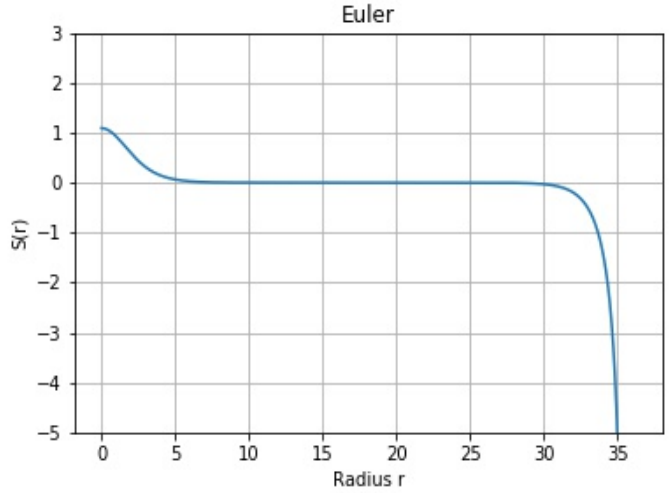

Figure 3.4: First bound-state wavefunction with $S_0 = 1.0890934531$, obtained using the Euler method, with $V_0 = 1$.

We have successfully solved the Schrodinger-Newton equations in the stationary case considering the spherically symmetric ground state configuration (3.10), leading us to the axion field and Newtonian potential. Now, we will be interested in clarifying the regimes for which our solutions will be stable or unstable. Two different quantities will be crucial for this aim: the number of particles $N = 4\pi \int_0^\infty dr'\, r'^2 \psi(r')^2$ and the clump size R. They will be plotted in the so-called *phase diagram*, providing a picture of the stability and instability regimes for our solutions. Eventually, when we include self-interactions, these diagrams will capture other relevant properties for these clumps such as the possible maximum values for this particle number, acting as a frontier for the existence of such compact objects. They will be constructed both analytically and numerically.

These axion field, obtained for diverse V_0, will lead us to the numerical part of the phase diagram. Anyway, first, we are going to consider different ansatzs for the radial part of the solution $\psi(r)$. Once introduced in the Hamiltonian, this one will lead us to an analytical version for the phase diagram.

As explained before, considering the spherical symmetry of the ground state (3.10) and solving the trivial angular integrals, the first term of the Hamiltonian (3.3) takes the form

$$H_{kin} = \frac{2\pi}{m_a} \int_0^\infty dr\; r^2 \left(\frac{d\psi}{dr}\right)^2 . \tag{3.29}$$

Obviously H_{int}, as we do not have self-interactions in this case, does not appear here but will be a prominent feature of the next section.

A slightly more complicated situation concerns the remaining part of this Hamiltonian, H_{grav}. In this case, as done in [16], the inverse distance is treated by means of the spherical expansion

$$\frac{1}{|\mathbf{x}-\mathbf{x}'|} = \sum_{l=0}^{\infty} \frac{4\pi}{2l+1} \left(\frac{r_<^l}{r_>^{l+1}} \right) \sum_{m=-l}^{l} Y_l^{m*}(\theta,\varphi) Y_l^*(\theta',\varphi') \tag{3.30}$$

being $r_<$ and $r_>$ the lesser and greater $r = |\mathbf{x}|$ and $r' = |\mathbf{x}'|$ respectively. The gravitational term in the Hamiltonian will be substantially simplified taking into account that the angular integrals eliminate all the terms but the one with $l = m = 0$, leading us to

$$H_{grav} = -8\pi^2 G m_a^2 \int_0^\infty dr\ r^2 \int_0^\infty dr'\ r'^2 \frac{\psi(r)^2 \psi(r')^2}{r_<}. \tag{3.31}$$

Now, let us consider three different ansatzs for $\psi(r)$. Before starting, it is important to stress that they will only give us a qualitative idea of the behaviour of the system. The degree of precision of each of them will be clarified in a direct comparison with the numerical result. For a deeper review of most of the different ansatzs appearing in the literature see [30].

In particular we will take into account a simple *exponential* ansatz, a *hyperbolic secant* ansatz, and a *linear + exponential* ansatz, which will be, respectively

$$\psi_R(r) = \sqrt{\frac{N}{\pi R^3}} \exp\left(-r/R\right), \tag{3.32}$$

$$\psi_R(r) = \sqrt{\frac{3N}{\pi^3 R^3}} \mathrm{sech}(r/R), \tag{3.33}$$

$$\psi_R(r) = \sqrt{\frac{N}{7\pi R^3}} (1 + r/R) \exp\left(-r/R\right) \tag{3.34}$$

where the prefactors multiplying each of them ensure that $N = 4\pi \int_0^\infty dr\ r^2 \psi(r)^2$ and R is left free and acts as a variational parameter.

Let us try to clarify how good these solutions are for different small and big values of r. We are going to compare the different ansatzs with the exact numerical result obtained from solving numerically the system of coupled equations (3.22) and (3.23). For this aim, it will be necessary to set the same N value for the all ansatzs but also for the numerical result.

As it can be seen in Figure 3.5, the exponential ansatz is not a good approximation when $r \to 0$. On the other hand, the hyperbolic secant and linear + exponential ansatzs get closer to numerical result in this regime, being also really similar between themselves.

Our next step is the introduction of these ansatzs in each of the three terms of the Hamiltonian. Then, solving the integrals, we will be able to obtain the explicit form of H for each ansatz. For example, in the case of the exponential ansatz, we obtain

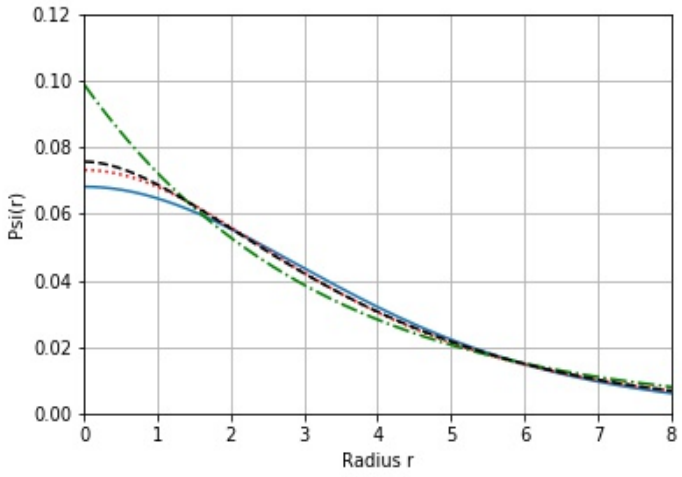

Figure 3.5: The dimensionless axion field $\tilde{\psi}(r)$ for the different ansatzs versus the dimensionless radius $\tilde{r}$, together with the numerical result obtained in the previous section. The exponential ansatz is represented by lined dotted green plot, the dashed black line stands for the linear + exponential ansatz, the dotted red line represents the hyperbolic secant ansatz and finally, the solid blue line stands for the numerical result. They are all normalized, in such a way that $\tilde{N} = 1$.

$$H(R) = \frac{N}{2m_a R^2} - \frac{5Gm_a^2 N^2}{16R}, \tag{3.35}$$

where the first term corresponds to the kinetic term (3.29) and the second one to the gravitational term (3.31).

In order to simplify our analysis, it will be better to work with the dimensionless version of this Hamiltonian, $\tilde{H}$, considering also the dimensionless clump size $\tilde{R}$ and the dimensionless particle number $\tilde{N}$, needed also for the dimensionless version of each axion field ansatz represented in Figure 3.5. They are defined through the relations

$$\tilde{H} \equiv \frac{m_a}{\sqrt{G}} H, \tag{3.36}$$

$$\tilde{N} \equiv m_a^2 \sqrt{G} N, \tag{3.37}$$

$$\tilde{R} \equiv m_a \sqrt{G} R. \tag{3.38}$$

The final dimensionless version of the Hamiltonian for the exponential ansatz will be

$$\tilde{H}(\tilde{R}) = \frac{\tilde{N}}{2\tilde{R}^2} - \frac{5\tilde{N}^2}{16\tilde{R}}. \tag{3.39}$$

In fact, the shape of the Hamiltonian for each of the other two ansatzs will be really similar. As expected they all share the same two terms, with the same powers of $\tilde{N}$ and $\tilde{R}$ in the numerator and denominator, but different coefficients,

$$\tilde{H}(\tilde{R}) = a\frac{\tilde{N}}{\tilde{R}^2} - b\frac{\tilde{N}^2}{\tilde{R}}, \tag{3.40}$$

where

$$a = \frac{12 + \pi^2}{6\pi^2},\ b = \frac{6(12\zeta(3) - \pi^2)}{\pi^4},\ \text{(sech ansatz)}, \tag{3.41}$$

$$a = \frac{3}{14},\ b = \frac{5373}{25088},\ \text{(linear + exp. ansatz)}. \tag{3.42}$$

In Figure 3.6, the dimensionless Hamiltonian $\tilde{H}$ for each of the ansatzs is shown. The local minimum appearing in the Hamiltonian tell us that the bound state solution previously obtained is in fact physically stable. When self-interactions are included, a maximum linked with an unstable solution will appear, as we will see in the next section. Also notice that the shape of $\tilde{H}$ coincides for the three ansatzs.

At last, extremazing $\tilde{H}$ with respect to $\tilde{R}$ leads us to

$$\tilde{R} = \frac{5}{16\tilde{N}}, \tag{3.43}$$

for the exponential ansatz.

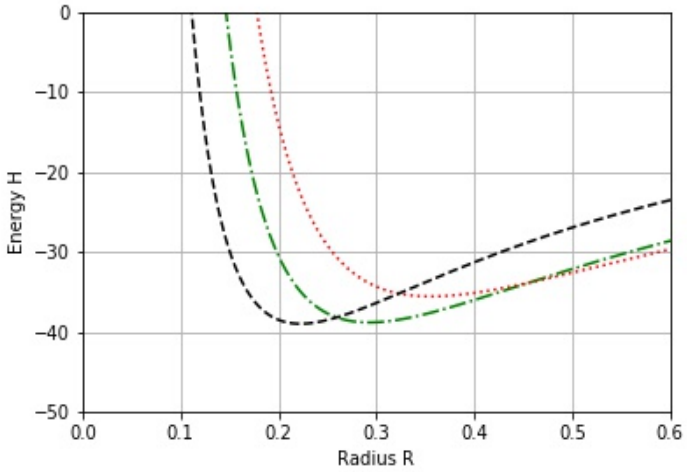

Figure 3.6: Representation of the Hamiltonian $\tilde{H}$ for the different ansatzs versus the dimensionless clump size $\tilde{R}$ in the case without self-interactions. The exponential ansatz is represented by lined dotted green line, the dashed black line stands for the linear + exponential ansatz, the dotted red line represents the hyperbolic secant ansatz. Here $\tilde{N} = 9$.

On the other hand,

$$\tilde{R} = \frac{2a}{b\tilde{N}}, \tag{3.44}$$

stand for the sech and linear + exponential ansatzs.

As commented before, apart from the analytical results (3.43) and (3.44), we will include exact numerical ones represented by individual dots in Figure 7, obtained by solving the Schrodinger-Newton equations (3.22) and (3.23) for different values of V_0. The numerical values relative to each individual black point in Figure 7 are shown in Table 3.2, together with the particular values of S_0 and V_0. Remember that, when the axion field $S(r)$ was obtained previously by solving numerically the Schrodinger-Newton equations, the V_0 remained fixed during the process, arbitrarily set equal one.

The calculation of the dimensionless particle number is straightforward. Considering its definition

$$N = 4\pi\alpha^2 \int_0^\infty dr'\ r'^2 S(r')^2, \tag{3.45}$$

with α previously defined (3.17), all we have to do is to solve the integral numerically, for what we have used a composite trapezoidal rule. Notice that this is not the first time $\tilde{N}$ is obtained, as it has been already calculated in the normalization of the results appearing in Figure 3.5, for instance.

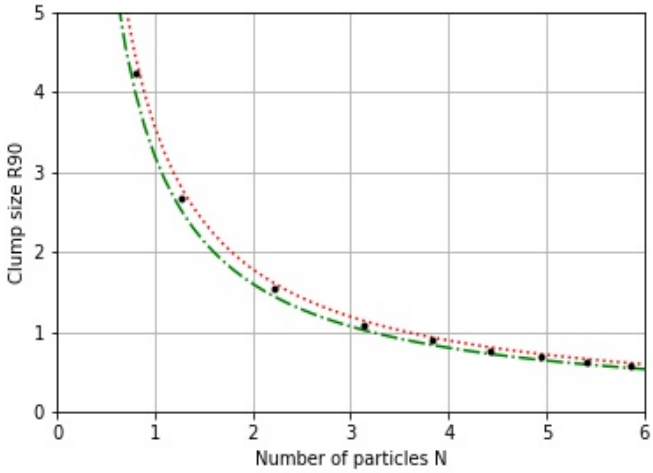

Figure 3.7: Phase diagram ($\tilde{R}_{90}$ versus $\tilde{N}$) in the case without self-interactions, obtained analytically for the exponential ansatz, represented by lined dotted green line, and for the hyperbolic secant ansatz shown as a red dotted line. The black individual dots stand for the numerical result, obtained solving the Schrodinger-Newton equations for different V_0 values, see Table 3.2 for further details.

In general, our phase diagrams will be a representation of the dimensionless particle number $\tilde{N}$, already defined, versus the dimensionless radius enclosing 90% of the mass, defined by means of the relation

$$0.9N = 4\pi\alpha^2 \int_0^{R_{90}} dr'\ r'^2 S(r')^2. \tag{3.46}$$

Also, remember that, when we discussed the analytical part of these phase diagrams, in equations such as (3.43) or (3.44), we obtained originally a relation between $\tilde{N}$ and $\tilde{R}$. However, in Figure 6, we consider instead $\tilde{R}_{90}$ versus $\tilde{N}$, so a relation between $\tilde{R}$ and $\tilde{R}_{90}$ has been needed for each ansatz. They are easily obtained by substituting the different ansatzs in (3.46), leading us to

$$\tilde{R}_{90} \approx 2.661\tilde{R} \ \text{(exponential ansatz)}, \tag{3.47}$$

$$\tilde{R}_{90} \approx 2.799\tilde{R} \ \text{(sech ansatz)}. \tag{3.48}$$

Now that we have fully studied the case with negligeble self-interactions, we are going to repeat the analysis including them at different orders and in diverse forms.

$\tilde{R}_{90}$	$\tilde{N}$	V_0	S_0
4.223	0.80899	0.4	0.615872
2.67	1.27896	1	1.5397453
1.541	2.21466	3	4.619632
1.089	3.13121	9	9.2400418
0.889	3.8342	12	18.4822873
0.77	4.42665	15	23.103971
0.689	5.42005	18	27.7259724
0.629	5.85363	21	32.3482641
0.582	6.25711	24	36.9708246

Table 3.2: Detail of the numerical values represented as individual black dots in Figure 3.7

3.3 Quartic Self-interactions

The self-interaction potential considered in this section, is the already introduced (3.2). It arises when we consider the naive non-relativistic reduction at first order. As it was shown previously by means of axion EFT, this naive reduction only leads to the right coefficient at this leading order.

Our first step will be finding solutions for the Schrodinger-Newton system of equations (this time (3.11) and (3.12)) using once again the method suggested by Moroz et al. for the previous case.

We introduce then the redefinition $U(r) \equiv E - \varphi_N(r)$. For numerical purposes, we are going to work with a system of four first order coupled differential equations instead of the two second order coupled differential equations system. After certain calculations we have

$$\tilde{\psi}_r' = -\frac{2}{\tilde{r}}\tilde{\psi}_r - 2\tilde{U}\psi - \frac{1}{4}|\tilde{\psi}|^2\tilde{\psi}, \tag{3.49}$$

$$\tilde{U}_r' = -\frac{2}{\tilde{r}}\tilde{U}_r - 4\pi|\tilde{\psi}|^2, \tag{3.50}$$

where

$$\tilde{\psi}_r = \tilde{\psi}', \tag{3.51}$$

$$\tilde{U}_r = \tilde{U}', \tag{3.52}$$

being the prime, once again, derivative over the radius $\tilde{r}$. As in the original equations (3.11) and (3.12), the variables with tilde are dimensionless.

At this stage, we apply the process introduced in the previous subsection. As bound states are expected to be placed between a solution for which $(\tilde{\psi}, \tilde{U}) \longrightarrow (+\infty, -\infty)$ (we will refer to this kind once again as $(+,-)$ solution) and another with $(\tilde{\psi}, \tilde{U}) \longrightarrow$

$(-\infty, -\infty)$ (which will be also called $(-,-)$ solution). Setting $\tilde{U}_0 = 1$, the bound state will be determined calculating the value of $\tilde{\psi}_0$ with arbitrary precision, as previously done with S_0 and V_0. Now, let us analyze the solutions obtained and compare them with the previous case.

The first difference introduced by this extra self-interaction term is related with how our solutions diverge. While the value of $\tilde{\psi}(r)$ grows, the last term in (3.11) or the self-interaction term, gets more relevant. Then, we do not have just a simple exponential divergence, as in the previous case, but when $\tilde{\psi}(r)$ gets big enough an oscillatory behaviour on top of the exponential divergence. The shape of this divergence is shown in Figure 3.9. In essence, this behaviour does not change our treatment, as in fact solutions are clearly blowing up to positive or negative values and bound states have been found numerically where expected, in the point where the divergent behaviour changes, as detailed below.

The second difference, crucial for our future discussion, lies in the fact that not only one but two solutions are found for each bound state. To avoid confusion, let us focus only in the first bound state. As in the previous section, if we start increasing $\tilde{\psi}_0$ (always with fixed $\tilde{U}_0 = 1$) from values close to zero, at the beginning all the solutions will be $(-,-)$. At certain $\tilde{\psi}_0$, as happened before in the transition from $S_0 = 1.08$ to $S_0 = 1.09$, a $(+,-)$ solution appears. Then, a bound state is expected between these two solutions with opposite behaviour in the divergence, as explained before. Following the path introduced for the previous case, the particular value of $\tilde{\psi}_0$ for this bound state may be calculated up to the desired precision. See Figure 3.8 for further details.

In the case without self-interactions, if once we have $(+,-)$ solutions we continue increasing the value of S_0, we find only solutions with $S(r)$ diverging to $+\infty$. On the other hand, when the self-interaction term is included and we increase enough the value of $\tilde{\psi}_0$, at a certain point the behaviour of the solutions changes once again, and above it, for any value of $\tilde{\psi}_0$, we will only find $(-,-)$ solutions. As before, this transition is linked with the existence of an extra bound state shown in Figure 3.9.

A couple of extra comments are necessary. First of all, we will refer to this new extra solution as *unstable solution*, while the former one, also appearing in the case without self-interactions, is the so-called *stable solution*. Here we are discussing the already introduced physical stability and, linked with the time evolution of these solutions. In [16] after perturbing away the solutions by a small finite amount, time evolution of both of them is tracked. While physically stable solutions merely oscillate, independently of the sign of the perturbation, the physically unstable solution runs away. Note, once again, that this has nothing to do with the mathematical instability, related with the infinite precision in S_0 or $\tilde{\psi}_0$ to find a non divergent bound state solution.

Also here, by means of the introduction of different ansatzs for the axion field, we will be able to find an analytical expression for the Hamiltonian. This one will show a local maximum linked with the already mentioned unstable solution and a local minimum related with the stable solution, now that a self-interaction term has been included.

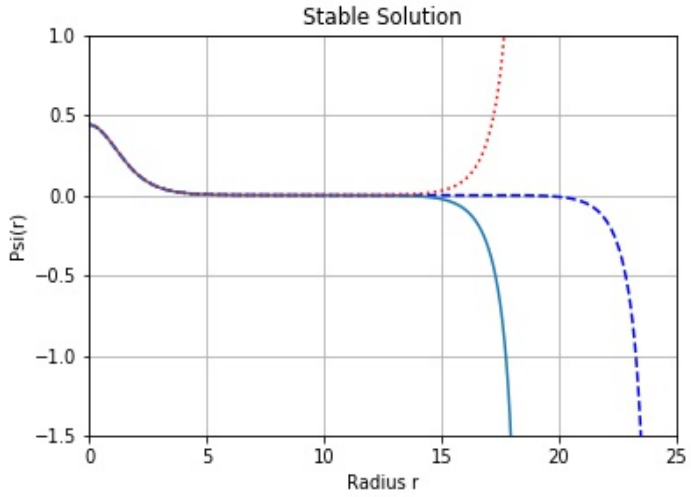

Figure 3.8: The red dotted line represents the first bound-state wavefunction with $\tilde{\psi}_0 = 0.4394655$, while the solid blue line stands for the first bound-state wavefunction with $\tilde{\psi}_0 = 0.4394654$. The solution represented by a dashed blue line has instead a $\tilde{\psi}_0 = 0.4394654657$. This is the so-called *stable solution*. All of them have been obtained using the Runge-Kutta method.

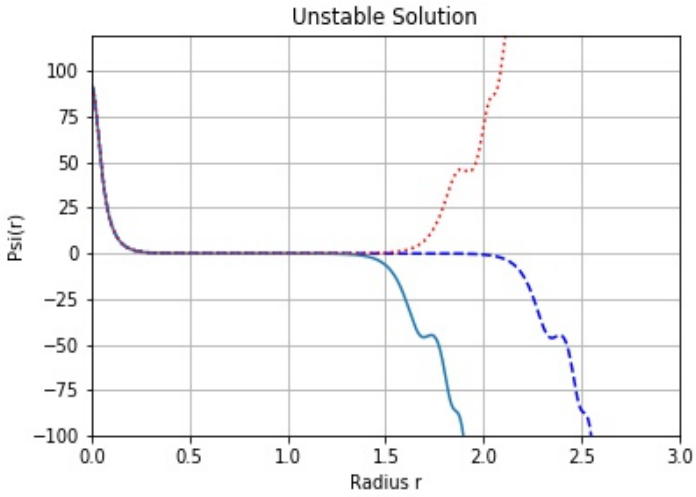

Figure 3.9: The red dotted line represents the first bound-state wavefunction with $\tilde{\psi}_0 = 91.7158035$, while the solid blue line stands for the first bound-state wavefunction with $\tilde{\psi}_0 = 91.7158036$. The solution represented by a dashed blue line has instead a $\tilde{\psi}_0 = 91.7158035591$. This is the so-called *unstable solution*. All of them have been obtained using the Runge-Kutta method.

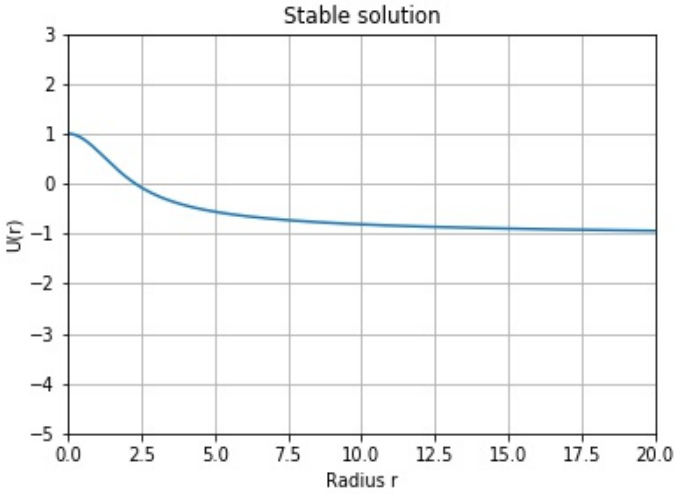

Figure 3.10: Newtonian potential $\tilde{U}(r)$ with $\tilde{\psi}_0 = 0.4394654657$, being $U_0 = 1$, obtained using the Runge-Kutta method.

At last, notice than the Newtonian potential $\tilde{U}(r)$ keep the expected monotonically decreasing shape, as it is shown in Figure 3.10 and Figure 3.11.

Now, let us focus our efforts in obtaining and studying the analytical Hamiltonian and the phase diagram. In particular, we will construct the latter both analytically, by means of different ansatzs and approximations, and numerically.

The terms of the Hamiltonian in which we are going to substitute the different ansatzs will be (3.29) and (3.31), but with the contribution of an extra term directly related with the self-interaction term which, considering the spherically symmetric ground state configuration (3.10), takes the form

$$H_{int} = 4\pi \int_0^\infty dr\ r^2\, V_{naive}(\psi). \tag{3.53}$$

The next step is the introduction of the ansatzs (3.32), (3.33) and (3.34) in each of the three terms of the Hamiltonian (3.3). Then, solving the integrals, we will be able to obtain the explicit form of H_{naive} for each ansatz. For example, in the case of the exponential ansatz, we obtain

$$H_{naive}(R) = \frac{N}{2m_a R^2} - \frac{5Gm_a^2 N^2}{16R} - \frac{N^2}{128\pi f^2 R^3} \tag{3.54}$$

where the first addend corresponds to the kinetic term (3.29), the second one to the gravitational term (3.31) and the third one to the interaction term (3.53).

In order to simplify our analysis, it will be better to work with the dimensionless

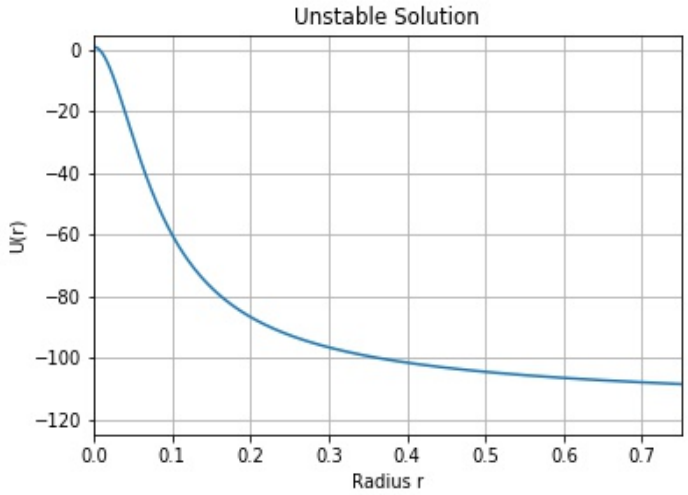

Figure 3.11: Newtonian potential $\tilde{U}(r)$ with $\tilde{\psi}_0 = 91.7158035591$, being $U_0 = 1$, obtained using the Runge-Kutta method.

version of this Hamiltonian, $\tilde{H}$, considering also the dimensionless clump size $\tilde{R}$ and the dimensionless particle number $\tilde{N}$. They are defined as

$$\tilde{H}_{naive} \equiv \frac{m_a}{f^3\sqrt{G}} H_{naive}, \tag{3.55}$$

$$\tilde{N} \equiv \frac{m_a^2\sqrt{G}}{f} N, \tag{3.56}$$

$$\tilde{R} \equiv m_a f \sqrt{G} R. \tag{3.57}$$

The final dimensionless version of the Hamiltonian for the exponential ansatz will be

$$\tilde{H}_{naive}(\tilde{R}) = \frac{\tilde{N}}{2\tilde{R}^2} - \frac{5\tilde{N}^2}{16\tilde{R}} - \frac{\tilde{N}^2}{128\pi\tilde{R}^3}. \tag{3.58}$$

In fact, the shape of the Hamiltonian for each of the other two ansatzs will be rather similar. As expected they all share the same three terms, with the same powers of $\tilde{N}$ and $\tilde{R}$ in the numerator and denominator, but different coefficients. For the remaining two ansatzs, we have

$$\tilde{H}_{naive}(\tilde{R}) = a\frac{\tilde{N}}{\tilde{R}^2} - b\frac{\tilde{N}^2}{\tilde{R}} - c\frac{\tilde{N}^2}{\tilde{R}^3}. \tag{3.59}$$

where the coefficients a and b have been previously introduced in (3.41) and (3.42) and the coefficient c is

$$c = \frac{\pi^2 - 6}{8\pi^5} \quad \text{(sech ansatz)}, \tag{3.60}$$

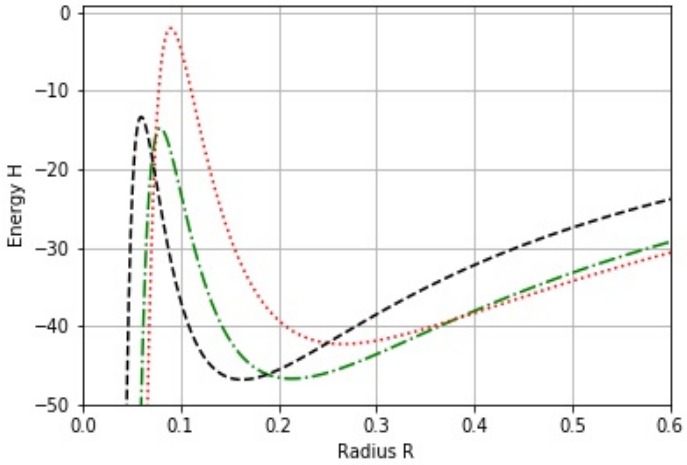

Figure 3.12: Representation of the Hamiltonian $\tilde{H}$ for the different ansatzs versus the dimensionless clump size $\tilde{R}$ in the case with a single self-interaction term. The exponential ansatz is represented by lined dotted green line, the dashed black line stands for the linear + exponential ansatz, the dotted red line represents the hyperbolic secant ansatz. Here $\tilde{N} = 9$.

$$c = \frac{437}{200704\pi} \quad \text{(linear + exp. ansatz)}. \tag{3.61}$$

In Figure 3.12 the analytical Hamiltonian for each ansatz is shown. As expected their shapes are very similar, with a local maximum linked with the unstable solution and a local minimum related with the stable solution.

At last, we are going to extremize $\tilde{H}$ with respect to $\tilde{R}$. In the case with self-interaction term and for the exponential ansatz, we have

$$\tilde{R} - \frac{5}{16}\tilde{N}\tilde{R}^2 - \frac{3}{128\pi}\tilde{N} = 0. \tag{3.62}$$

Its solutions will be

$$\tilde{R} = \frac{8}{5\tilde{N}} \pm \frac{\sqrt{512\pi - 15\tilde{N}^2}}{10\sqrt{2\pi}\tilde{N}}. \tag{3.63}$$

On the other hand, for the other two ansatzs the solutions will be instead

$$\tilde{R} = \frac{a \pm \sqrt{a^2 - 3bc\tilde{N}^2}}{b\tilde{N}}, \tag{3.64}$$

being a, b and c the already introduced coefficients (3.41), (3.42), (3.60) and (3.61).

At first sight, we notice that these solutions are going to present a maximum value of $\tilde{N}$ being

$$\tilde{N}_{max} = \sqrt{\frac{512\pi}{15}} \approx 10.36, \tag{3.65}$$

in the exponential case and

$$\tilde{N}_{max} = \frac{a}{\sqrt{3bc}}, \tag{3.66}$$

for the other two ansatzs, giving $\tilde{N}_{max} \approx 10.12$ for the hyperbolic secant and $\tilde{N}_{max} \approx 10.15$ for the linear + exponential.

Together with these analytical results we will include the exact numerical ones in the phase diagram, represented as black individual dots in Figure 3.13. To obtain them, we are going to use the axion field $\psi(r)$, solution of the Schrodinger-Newton equations (3.11) and (3.12) that we have just obtained.

The calculation of the dimensionless particle number is straightforward. Considering its definition

$$\tilde{N} = 4\pi \int_0^\infty d\tilde{r}' \; \tilde{r}'^2 \tilde{\psi}(\tilde{r}')^2, \tag{3.67}$$

all we have to do is to solve it numerically, for what we have used again a composite trapezoidal rule.

On the other hand, the dimensionless radius enclosing 90% of the mass will be

$$0.9\tilde{N} = 4\pi \int_0^{\tilde{R}_{90}} d\tilde{r}' \; \tilde{r}'^2 \tilde{\psi}(\tilde{r}')^2. \tag{3.68}$$

In order to obtain each exact numerical value represented by an individual dot in Figure 3.13, explicitly shown in Table 3.3 and Table 3.4 together with the initial values of $\tilde{\psi}(r)$ and $\tilde{U}(r)$, we will consider different values of $\tilde{U}_0$. Remember that, when the axion field was originally obtained at the beginning of this section by solving numerically the Schrodinger-Newton equations, this value remained fixed during the process, arbitrarily set equal one.

To clarify these diagrams some comments are necessary. First of all, color have been used to distinguish the stable solutions, appearing in the diagram for bigger clump sizes, in blue an unstable solutions and with a smaller $\tilde{R}_{90}$ in red. As can be seen in Figure 3.13, the hyperbolic secant ansatz gets values closer to the exact numerical ones, at least for the stable branch.

To conclude this section, lets transform back some dimensionless quantities to their original form, in order to have a more clearer physical picture of the results obtained. In particular we will consider the mass and the PQ scale of the QCD axion. For instance, the maximum number of particles already defined and the relative maximum mass are

$$N_{max} = \frac{f}{m_a^2\sqrt{G}}\tilde{N}_{max} \sim 8 \times 10^{59}(\tilde{m}_a^{-2}\tilde{f}), \tag{3.69}$$

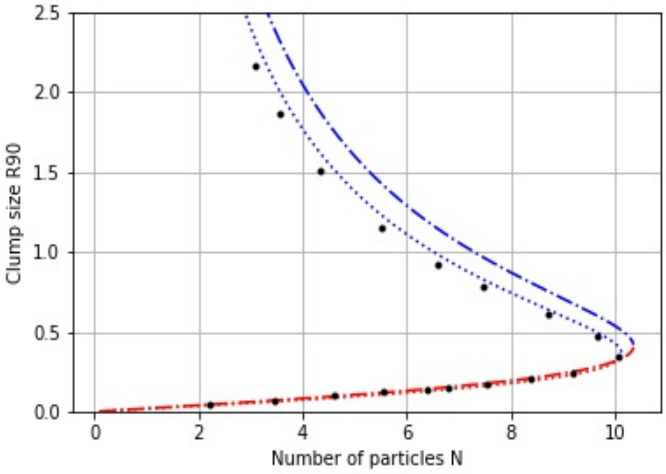

Figure 3.13: Phase diagram ($\tilde{R}_{90}$ versus $\tilde{N}$) in the case with a single self-interaction term, obtained analytically for the exponential ansatz, represented by lined dotted line, and for the the hyperbolic secant ansatz shown as a dotted line. While in blue we represent the stable branch of solutions, the red lines stand for the unstable ones. The black individual dots stand for the numerical result, obtained solving the Schrodinger-Newton equations for different $\tilde{U}_0$ values. See Table 3.3 and Table 3.4 for further details.

$\tilde{R}_{90}$	$\tilde{N}$	$\tilde{U}_0$	$\tilde{\psi}_0$
2.157	3.09773	1.5	0.6620276
1.861	3.56318	2	0.8875352
1.508	4.33009	3	1.3461569
1.15	5.50151	5	2.295703
0.92	6.5993	7.5	3.5495011
0.78	7.45564	10	4.8882538
0.606	8.708	15	7.8822804
0.477	9.64544	21	12.2687743
0.346	10.07969	29.5	21.6400533

Table 3.3: Detail of the numerical values represented as individual black dots in Figure 3.13 for the stable branch of solutions.

$$M_{max} = m_a \tilde{N}_{max} \sim 1.4 \times 10^{22} \text{ g } (\tilde{m}_a^{-1} \tilde{f}), \tag{3.70}$$

where $\tilde{f} \equiv f/(6 \times 10^{11})$ GeV and $\tilde{m}_a \equiv m_a/(6 \times 10^{-5})$ eV.

On the other hand, the minimum clump size for the stable branch (represented in blue in Figure 3.13) will be

$$R_{90,min} = \frac{a}{bGm_a^3 \tilde{N}_{max} \tilde{R}} \tilde{R}_{90,min} \sim 1.3 \times 10^5 \text{ m } (\tilde{m}_a^{-1} \tilde{f}^{-1}). \tag{3.71}$$

In this section, we have first reproduced the results exposed in [28] and extended their analysis studying the stability of the bound state solution arising by means of the analytical Hamiltonian and the phase diagram. However, we have fully reproduced the results in [16] but obtaining the solutions for the Schrodinger-Newton system of equations using a different method and studying their stability with the analytical Hamiltonian.

Now, we are free to extend this analysis to more complicated potentials, specially to cases which describe more accurately the axion self-interactions in this regime, as the effective potential arising from axion EFT.

3.4 Other Self-interaction Potentials

At this stage, we have successfully studied the physical stability, by means of the phase diagrams and the local extremes in the analytical Hamiltonian, of the axion stars in the cases with negligible self-interactions and with the naive self-interaction potential just at first order. The natural next step is to consider other more complicated effective potentials, containing higher order terms, and repeat our analysis, allowing us to go beyond the cases already studied in the literature. We are going to do it via the analysis of two different effective potentials.

$\widetilde{R}_{90}$	$\widetilde{N}$	$\widetilde{U}_0$	$\widetilde{\psi}_0$
0.2389	9.17295	34	40.0000817
0.203	8.36681	32	51.0870249
0.1746	7.53233	26	63.2597965
0.1532	6.79272	17	75.4744423
0.1422	6.38114	10	83.132929
0.1217	5.56302	-10	100.9640338
0.0995	4.61121	-50	128.3146132
0.0742	3.47762	-150	178.1476512
0.0468	2.20487	-500	290.7992029

Table 3.4: Detail of the numerical values represented as individual black dots in Figure 3.13 for the unstable branch of solutions.

In the first part of this section we will consider the effective potential of a generic scalar field introduced by Mukaida et al. [19], going beyond axion stars to consider the more generic case of a real scalar star. As this potential will contain two self-interaction terms, we are going to get a feel for the effect of higher order corrections, being crucial the relative sign of the different self-interaction terms.

Then, in the second part we will go back to the effective self-interaction potential (2.11), derived using EFT matching methods, which gives us a much more accurate picture of the axion self-interactions. At last, we will compare the stability regimes in this case with the ones obtained considering higher order terms in the naive self-interaction potential (2.7), proving that, the later suggests the existence of a branch of dense axion stars which do not arise when considering the proper effective self-interaction potential.

3.4.1 Generic Scalar Field Potential

In this subsection we will consider a potential introduced in [19]. At the higher momentum regime, where a real scalar field $\phi(x)$ is more appropriate for our analysis, the potential takes the form

$$V(\phi) = \frac{g_3}{3}\phi^3 - \frac{g_4}{4}\phi^4 + \frac{g_6}{6}\phi^6, \tag{3.72}$$

being g_3, g_4 and g_6 dimensionless coupling constants.

Before applying the non-relativistic reduction and obtaining its form in the regime of our interest, it is important to stress that this is not the potential of an axion field, but a generic scalar field of mass m.

The effective potential obtained after the non-relativistic reduction by means of the MTY effective field theory, as a function of the complex scalar field $\psi(x)$, will be

$$V_{eff}(\psi^*\psi) = \left[-\frac{5g_3^2}{12m^2} - \frac{3g_4}{8}\right](\psi^*\psi)^2 + \left[\frac{5g_6}{24} + \frac{g_4^2}{128m^2}\right](\psi^*\psi)^3. \tag{3.73}$$

First of all, as we are interested mainly in theories with Z_2 symmetry, we will take $g_3 = 0$, in such a way that the final expression for the effective potential that will be considered is

$$V_{eff}(\psi^*\psi) = -\frac{3g_4}{8}(\psi^*\psi)^2 + \left[\frac{5g_6}{24} + \frac{g_4^2}{128m^2}\right](\psi^*\psi)^3. \tag{3.74}$$

Notice that, for a suitable value of g_4, we could end up having the self-interaction potential of the previous section plus a higher order term.

Furthermore, the Schrodinger-Newton system of equations in this case will be

$$i\frac{\partial\tilde{\psi}}{\partial\tilde{t}} = -\frac{1}{2\tilde{r}}\frac{\partial^2}{\partial\tilde{r}^2}(\tilde{r}\tilde{\psi}) + \tilde{\varphi}_N\tilde{\psi} - \frac{3\tilde{g}_4}{4}|\tilde{\psi}|^2\tilde{\psi} + \left[\frac{5\tilde{g}_6}{8} + \frac{3\tilde{g}_4^2}{128}\right]|\tilde{\psi}|^4\tilde{\psi} \tag{3.75}$$

$$\frac{1}{\tilde{r}}\frac{\partial^2}{\partial\tilde{r}^2}(\tilde{r}\tilde{\varphi}_N) = 4\pi|\tilde{\psi}|^2, \tag{3.76}$$

As in earlier sections, we are going to be focused in the ground state configuration with spherically symmetry configuration, whose form will be once again (3.10)

$$\psi_g(r,t) = \psi(r)e^{-i\mu t},$$

being $\psi(r)$ purely radial and all the time dependence lies in the exponential.

Then, the system of coupled differential equations that we are going to solve, will be the one of the stationary case, that is

$$\tilde{E}\tilde{\psi} = -\frac{1}{2\tilde{r}}\frac{\partial^2}{\partial\tilde{r}^2}(\tilde{r}\tilde{\psi}) + \tilde{\varphi}_N\tilde{\psi} - \frac{3\tilde{g}_4}{4}|\tilde{\psi}|^2\tilde{\psi} + \left[\frac{5\tilde{g}_6}{8} + \frac{3\tilde{g}_4^2}{128}\right]|\tilde{\psi}|^4\tilde{\psi} \tag{3.77}$$

$$\frac{1}{\tilde{r}}\frac{\partial^2}{\partial\tilde{r}^2}(\tilde{r}\tilde{\varphi}_N) = 4\pi|\tilde{\psi}|^2. \tag{3.78}$$

For this process, we use once again the method introduced by Moroz et al. [28], making use of the redefinition $U(r) \equiv E - \varphi_N(r)$ too. It helps us, from a computational efficiency point of view, to transform the Schrodinger-Newton equations in a system of four first order differential equations, this is,

$$\tilde{\psi}_r' = -\frac{2}{\tilde{r}}\tilde{\psi}_r - 2\tilde{U}\psi - \frac{3\tilde{g}_4}{2}|\tilde{\psi}|^2\tilde{\psi} + \left[\frac{5\tilde{g}_6}{4} + \frac{3\tilde{g}_4^2}{64}\right]|\tilde{\psi}|^4\tilde{\psi}, \tag{3.79}$$

$$\tilde{U}_r' = -\frac{2}{\tilde{r}}\tilde{U}_r - 4\pi|\tilde{\psi}|^2, \tag{3.80}$$

being

$$\tilde{\psi}_r = \tilde{\psi}', \tag{3.81}$$

$$\tilde{U}_r = \tilde{U}', \tag{3.82}$$

with the primes denoting derivatives with respect to $\tilde{r}$.

Before continuing solving this system of equations, we have to fix the values of the dimensionless coupling constants $\tilde{g}_4$ and $\tilde{g}_6$. As we would like to compare directly the results of this section with the previously presented ones, the former coupling constant will be fixed in such a way that the coefficient of the third term in (3.77) and in (3.11) coincide, leading us to

$$\tilde{g}_4 = \frac{1}{6}. \tag{3.83}$$

On the other hand, the value of the other coupling constant, will be

$$\tilde{g}_6 \simeq -1.082577 \times 10^{-3}. \tag{3.84}$$

The reasons for the particular choice of this value will be clarified in the study of the local extremes of the analytical Hamiltonian later on.

What needs to be observed here is the fact that with these particular choices of the coupling constants $\tilde{g}_4$ and $\tilde{g}_6$, the self-interaction terms, this is the last two terms in (3.77) and (3.79), will present opposite signs. While the first self-interaction term is, as in the previous section, negative, the second one will be otherwise, positive.

Setting $\tilde{U}_0 = 1$ and varying $\tilde{\psi}_0$, the different solutions will diverge either to $(\tilde{\psi}, \tilde{U}) \longrightarrow (+\infty, -\infty)$ (named as $(+,-)$ solution) or $(\tilde{\psi}, \tilde{U}) \longrightarrow (-\infty, -\infty)$ (which will be also called $(-,-)$ solution). As in the case containing a single self-interaction term coming from the leading order in the naive potential, we start the process with a small value of $\tilde{\psi}_0$. As we increase it, the sign of the divergence of $\psi(r)$ change, going from a $(-,-)$ to a $(+,-)$ solution. This is related with the existence of a bound state solution, shown in Figure 3.14, and an infinite precision in the initial value of $\psi(r)$ is needed to avoid the divergence, what allow us to determine ψ_0 with high precision.

Above this bound state solution, a second one arises as expected. This time it lies between a $(+,-)$ and a $(-,-)$ solution, like in the already mentioned previous case. When the analytical Hamiltonian is introduced, a physically unstable solution will be identify, linked with the local maximum appearing on H. This bound state solution is shown in Figure 3.15.

Notice that the values of ψ_0 for the solutions represented in Figure 3.14 and Figure 3.15, are similar to the ones represented in Figure 3.8 and Figure 3.9. This is something expected considering that, in this new case with two self-interaction terms, the first is identical to the one appearing in (3.11), while the second presents a small coefficient $\tilde{g}_6$.

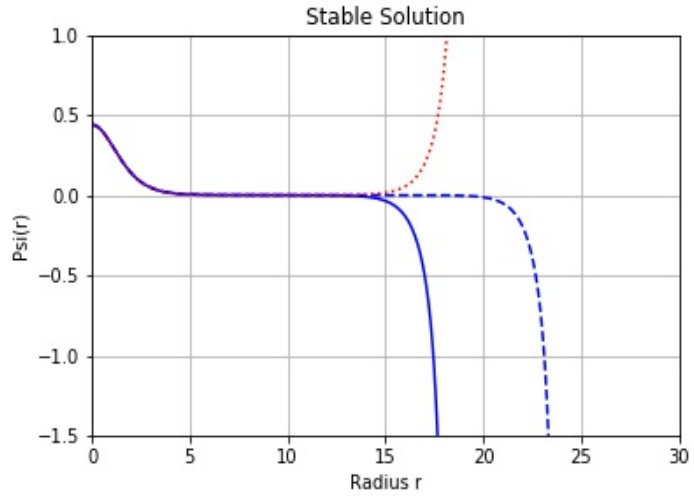

Figure 3.14: The red dotted line represents the first bound-state wavefunction with $\tilde{\psi}_0 = 0.4389736$, while the solid blue line stands for the first bound-state wavefunction with $\tilde{\psi}_0 = 0.4389735$. The solution with dashed blue line has instead a $\tilde{\psi}_0 = 0.4389735709$. This is the so-called *stable solution*. All of them have been obtained using the Runge-Kutta method.

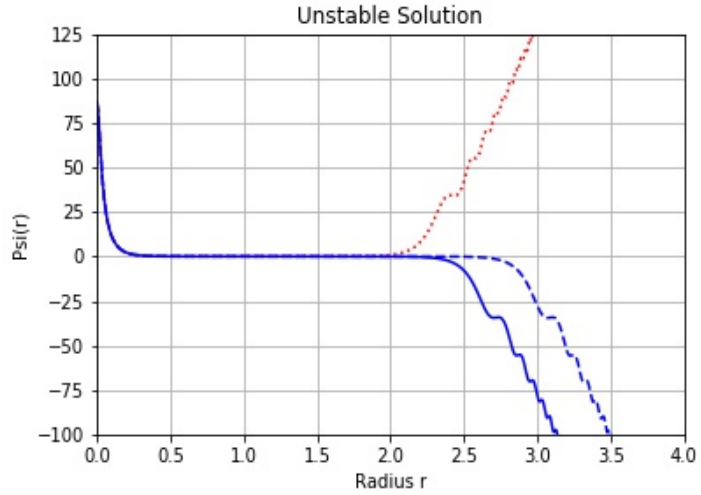

Figure 3.15: The red dotted line represents the first bound-state wavefunction with $\tilde{\psi}_0 = 86.4857618$, while the solid blue line stands for the first bound-state wavefunction with $\tilde{\psi}_0 = 86.4857619$. The solution with dashed blue line has instead a $\tilde{\psi}_0 = 86.4857618965$. This is the so-called *unstable solution*. All of them have been obtained using the Runge-Kutta method.

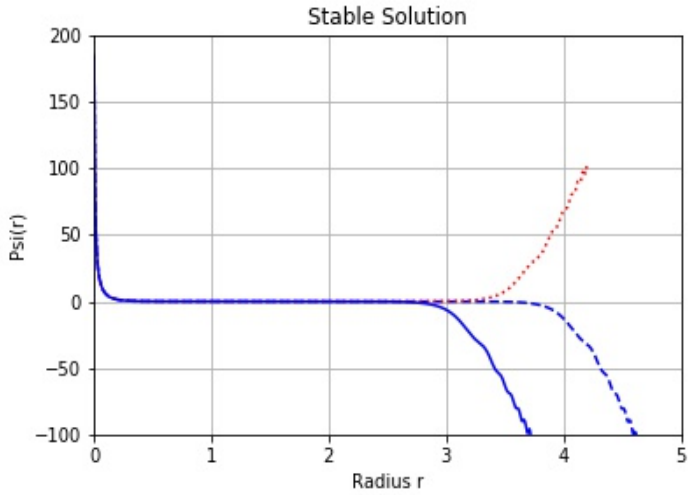

Figure 3.16: The red dotted line represents the first bound-state wavefunction with $\tilde{\psi}_0 = 184.101973$, while the solid blue line stands for the first bound-state wavefunction with $\tilde{\psi}_0 = 184.1019729$. The solution with dashed blue line has instead a $\tilde{\psi}_0 = 184.1019729976$. This is the new *dense stable solution*. All of them have been obtained using the Runge-Kutta method.

Even with this, an extra solution in this new case with a second self-interaction term of higher order appears once we have overcome this physically unstable bound state solution, represented in Figure 3.16. If we continue increasing the value ψ_0, we reach a new change in the behaviour of the solutions, going as initially, from a $(-,-)$ to a $(+,-)$ solution, what is related with the existence of other extra bound state solution which obviously does not appear in the case with a single self-interaction term. As demonstrated below, it is associated with a local minimum in the Hamiltonian and therefore considered a physically stable bound state solution. In general we will refer to these new stable solutions as *dense*. This is clarified in the study of the phase diagram, as they will have a lower R_{90} for the typical N values, if compered with the regular stable solutions.

Now, once that we have obtained these three bound state solutions, with the assumption spherical symmetry and with the previous shape for the time evolution in the ground state (3.10) we are going to consider the exponential ansatz for the radial part of the ground sate configuration

$$\psi_R(r) = \sqrt{\frac{N}{\pi R^3}} \exp\left(-r/R\right), \tag{3.85}$$

to obtain an analytical version of the Hamiltonian, which will allow us to study the physical stability of our solutions.

The Hamiltonian will be composed of three terms. While H_{kin} and H_{grav} take exactly the same form as in (3.29) and (3.31) respectively, H_{int} changes in this new case, as we have a different self-interaction potential. Introducing the ansatz and solving the equations we obtain

$$H(R) = \frac{N}{2mR^2} - \frac{5Gm^2N^2}{16R} - \frac{3g_4}{64\pi}\frac{N^2}{R^3} + (\frac{5}{648}g_6 + \frac{g_4^2}{3456m^2})\frac{N^3}{\pi^2R^6}, \tag{3.86}$$

where the last three terms arise from H_{int}. By means of the introduction of the dimensionless variables

$$\tilde{H} = \frac{G}{\sqrt{m}}H, \tag{3.87}$$

$$\tilde{N} = G\sqrt{m^3}N, \tag{3.88}$$

$$\tilde{R} = \sqrt{m^3}R, \tag{3.89}$$

$$\tilde{g_4} = \frac{m}{G}g_4, \tag{3.90}$$

$$\tilde{g_6} = \frac{m^4}{G^2}g_6 \tag{3.91}$$

we obtain a more simplified and dimensionless version of the previous equation

$$\tilde{H}(\tilde{R}) = \frac{\tilde{N}}{2\tilde{R}^2} - \frac{5\tilde{N}^2}{16\tilde{R}} - \frac{3\tilde{g_4}}{64\pi}\frac{\tilde{N}^2}{\tilde{R}^3} + (\frac{5\tilde{g_6}}{648\pi^2} + \frac{\tilde{g}_4^2}{3456\pi^2})\frac{\tilde{N}^3}{\tilde{R}^6}. \tag{3.92}$$

For the chosen values for the dimensionless coupling constants $\tilde{g}_4$ and $\tilde{g}_6$, our Hamiltonian will show three extremes when represented against $\tilde{R}$ in Figure 3.17. Once the value of $\tilde{g}_4$ was properly set, $\tilde{g}_6$ was chosen in such a way that $\tilde{H}$ shows the three local extremes. For example, when $\tilde{g}_6$ was slightly closer to zero, the maximum shows positive values.

The extra minimum appearing in $\tilde{H}$, suggests that the new stable bound solution is in fact physically stable. The other two extremes stand for the regular stable and unstable bound state solutions, as in the previous case with a single self-interaction term.

At last, lets consider the phase diagram. Extremising the Hamiltonian (3.92), we obtain

$$\frac{5}{16}\tilde{N}^2\tilde{R}^5 - \tilde{N}\tilde{R}^4 + \frac{9\tilde{g_4}}{64\pi}\tilde{N}^2\tilde{R}^3 - \left[\frac{15\tilde{g_6}}{324\pi^2} + \frac{\tilde{g}_4^2}{576\pi^2}\right]\tilde{N}^3 = 0, \tag{3.93}$$

taking the form shown in Figure 3.18. Comparing it with Figure 3.13, we see clearly the emergence of an extra branch of solutions previously identified as physically stable.

In general this section gives us a clear picture of the stability regimes of the scalar stars whose self-interaction potential takes the form (3.72). But another conclusion,

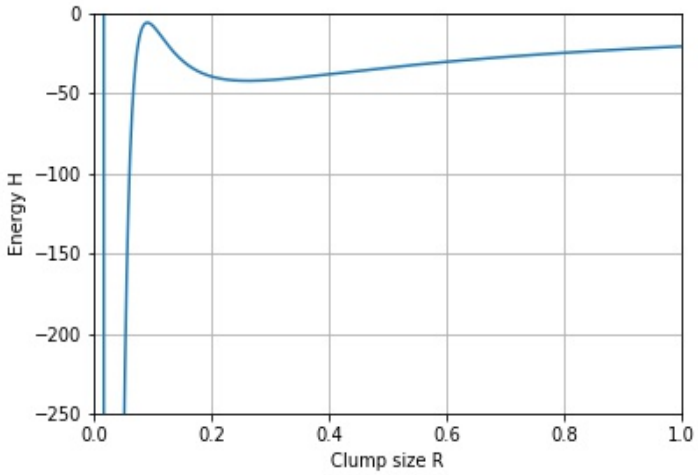

Figure 3.17: Representation of the Hamiltonian $\tilde{H}$ for the exponential ansatz versus the dimensionless clump size $\tilde{R}$ in the case with two self-interaction terms. Here $\tilde{N} = 9$. The first local minimum, associated with the new dense stable solution, is placed at $\tilde{H} \simeq -5391.88489$.

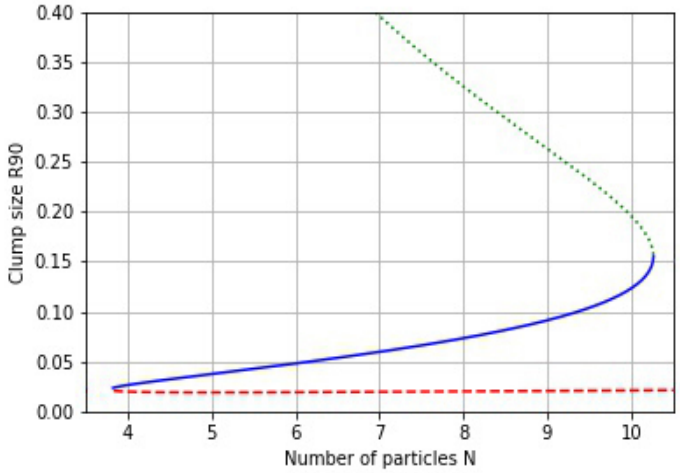

Figure 3.18: Phase diagram ($\tilde{R}_{90}$ versus $\tilde{N}$) in the case of a scalar field with two self-interaction term, obtained analytically from the exponential ansatz. The green dotted line represents the usual stable branch of solutions, the blue solid line represents the unstable branch of solutions while the dashed red line stands for the new dense stable branch of solutions.

central for the next part, we could come to, is that the existence of this extra dense branch of solutions is directly related to the fact that the two self-interaction terms in the effective potential have opposite signs.

3.4.2 Axion EFT Potential and Dense Axions Stars

In this section, returning to the axion field case, we will see how the naive non-relativistic reduction and in particular the sign of the coefficients of its effective potential, ends up suggesting the arising of an extra stable branch of solutions, in agreement with previous section conclusion, whose existence is refuted when the proper self-interaction potential is considered.

First of all, let us considering the already obtained self-interaction potential from axion EFT

$$\begin{aligned}\mathcal{V}_{eff}(\psi^*\psi) = \frac{\lambda_4}{16\, m_a f^2}(\psi^*\psi)^2 + \left[\lambda_6 - \frac{17}{8}\lambda_4^2\right]\left(\frac{(\psi^*\psi)^3}{288\, m_a f^4}\right) + \\ + \left[\lambda_8 - 11\lambda_4\lambda_6 + \frac{125}{8}\lambda_4^3\right]\left(\frac{(\psi^*\psi)^4}{9216\, m_a^2 f^6}\right) + \ \dots\ ,\end{aligned} \tag{3.94}$$

where m_a is the axion mass and the dots stand for higher order terms in the power-series expansion.

As in the relativistic regime, the axion self-interactions are mediated by the instanton potential (2.3), the power-series expansion of its cosine leads us to $\lambda_{2n} = (-1)^{n+1}$.

Our analysis here will be centred in the analytical Hamiltonian, once again obtained by means of the exponential ansatz. Concerning the effective potential, we will consider only the three terms explicitly shown in (3.94). Even though here we are truncating the power-series expansion, as we do it a order 8, this expansion will capture the behaviour of the cosine accurately.

First of all, within the spherically symmetric configuration, the ground state takes the typical form (2.10).

As occurred with the previous cases, we are only changing the effective potential, and subsequently only H_{int} will be different among the addends composing the Hamiltonian. As done before, the ansatz for the radial part $\psi(r)$ in each of the parts of H (3.4), (3.5) and (3.6) we obtain

$$\begin{aligned}H = \frac{N}{2m_a R^2} - \frac{5Gm_a^2N^2}{16R} + \frac{\lambda_4 N^2}{128\pi f^2 R^3} + \left[\lambda_6 - \frac{17}{8}\lambda_4^2\right]\frac{N^3}{7776\pi^2 m_a f^4 R^6} + \\ + \left[\lambda_8 - 11\lambda_4\lambda_6 + \frac{125}{8}\lambda_4^3\right]\frac{N^4}{589824\pi^3 m_a^2 f^6 R^9},\end{aligned} \tag{3.95}$$

where, as always, the first two terms correspond to H_{kin} and H_{grav} respectively, while the remaining terms are linked with H_{int}.

The common adimnesionlization process leads us to

$$\begin{aligned}\tilde{H}_{nr} = \frac{\tilde{N}}{2\tilde{R}^2} - \frac{5\tilde{N}^2}{16\tilde{R}} + \frac{\lambda_4\tilde{N}^2}{128\pi\tilde{R}^3} + \left[\lambda_6 - \frac{17}{8}\lambda_4^2\right]\frac{f^2G}{7776\pi^2}\frac{\tilde{N}^3}{\tilde{R}^6} + \\ + \left[\lambda_8 - 11\lambda_4\lambda_6 + \frac{125}{8}\lambda_4^3\right]\frac{f^4G^2}{589824\pi^3}\frac{\tilde{N}^4}{\tilde{R}^9},\end{aligned} \tag{3.96}$$

where the dimensionless variables are defined as

$$\tilde{R} \equiv mf\sqrt{G}R, \tag{3.97}$$

$$\tilde{N} \equiv \frac{m^2\sqrt{G}}{f}N, \tag{3.98}$$

$$\tilde{H} \equiv \frac{m}{f^3\sqrt{G}}H. \tag{3.99}$$

As a last step, we substitute the explicit values of λ_{2n}, leading us to

$$v_2 = \lambda_4 = -1, \tag{3.100}$$

$$v_3 = \lambda_6 - \frac{17}{8}\lambda_4^2 = -\frac{9}{8}, \tag{3.101}$$

$$v_4 = \lambda_8 - 11\lambda_4\lambda_6 + \frac{125}{8}\lambda_4^3 = -\frac{45}{8}. \tag{3.102}$$

and then

$$\tilde{H} = \frac{\tilde{N}}{2\tilde{R}^2} - \frac{5\tilde{N}^2}{16\tilde{R}} - \frac{\tilde{N}^2}{128\pi\tilde{R}^3} - \frac{f^2G}{6912\pi^2}\frac{\tilde{N}^3}{\tilde{R}^6} - \frac{45f^4G^2}{4718592\pi^3}\frac{\tilde{N}^4}{\tilde{R}^9}. \tag{3.103}$$

If we observe in detail the coefficients v_n here obtained and we compare them with the ones of the naive case $\lambda_{2n} \equiv (-1)^{n+1}$, the fundamental difference concerns v_3 and λ_6. While the former is negative, sharing the sign with the other two v_n shown, the latter is positive, contrary to λ_4 and λ_8.

This tells us that, if we perform our stability analysis considering the higher order terms in the naive effective potential we will always find an extra dense branch of solutions, usually called *dense axion stars*, as suggested by the result obtained in Section 3.4.1. However, these dense compact objects do not appear when the right non-relativistic reduction coming from axion EFT is considered, at least up to $n = 5$. As we have explained the sign of the coefficient v_3 leads us only to the existence of the regular stable and unstable branches, as it is easily deduced from the form of the Hamiltonian (3.103), with only two local extreme: a maximum and a minimum.

The discussion of the existence or not of these dense branch of solutions is one of the most controversial points in the recent literature concerning axion stars. While the existence of the common stable branch of solutions (whose associated compact objects are commonly called *dilute axion stars*) is clear, as it arises in a lower density regime where taking the leading order in the effective potential is justified, the situation is more complicated in the dense case, where the higher order terms in the power-series expansion get more relevant.

In [31] this dense axion star solution is discussed. Here, Braaten et al., consider the naive non-relativistic reduction (2.5) including the full cosine expansion in the potential, by means of

$$\mathcal{V}_{eff}(\psi^*\psi) = \frac{1}{2}m_a\psi^*\psi + m_a^2 f^2[1 - J_0(n^{1/2})] \tag{3.104}$$

where $n = 2\psi^*\psi/m_a f^2$ and $J_0(z)$ is a Bessel function. See [32] for further details in this expression. Here, in the dense axion stars regime, the Schrodinger-Newton equations take the form

$$\nabla^2\psi = -2m_a[\mu - (\mathcal{V}'_{eff}(\psi^*\psi) - m_a) - m_a\varphi_N]\psi, \tag{3.105}$$

$$\nabla^2\varphi_N = 4\pi G m_a\psi^*\psi. \tag{3.106}$$

where once again both ψ and φ_N are radial functions. For the study of this new branch, the Thomas-Fermi approximation was introduced, simplifying the treatment by eliminating the kinetic energy term, this is, the gradient in (3.105). As expected, considering that the effective potential (3.104) was obtained from the naive non-relativistic reduction, this extra stable branch of solutions arose (see Figure 1 in [31]).

However, Visinelli et al. [33] are in disagreement with the result in [31], as it is obtained within the Thomas-Fermi approximation, not valid in the regime where Brateen et al. expect dense scalar stars to appear. They state also that the single-harmonic approximation is not valid either here. This approximation was used in [16] as a first step in a discussion that concluded the existence of this extra dense branch of solutions.

What our work has shown is that the naive non-relativistic reduction is not valid beyond the leading order. We have seen that even at second order it produces a dense branch of solutions whose existence is refuted considering the self-interaction potential (3.94) up to this very same power instead. This generates doubts concerning the results in [31], as they are obtained with the power-series expansion of the cosine at all orders, after performing the naive non-relativistic reduction. A more accurate alternative, that we leave for future work, could be to consider higher orders in (2.11) to figure out if this dense branch of solutions arises at some point or if the behaviour that we have observed, with the different v_n sharing the same sign, remains.

Chapter 4

Summary and Conclusions

The axion, one of the favoured candidates to form the cold dark matter in the universe, may form compact objects called axion stars. The interplay between gradient energy, gravity and self-interactions gives rise to dilute and dense axion stars. Being more concrete, these objects are simply axion BEC, which justifies their study in the non-relativistic regime.

One of the most controversial points of the study of the axion field with momenta below the axion mass, lies in the non-relativistic reduction. Commonly in the literature, the process of redefining the real scalar field ϕ, representing the axion field in a higher momentum regime, by means of a scalar field ψ, which leads us to a simpler description below m_a, is performed through a naive non-relativistic reduction. Using effective field theory methods, the limitations of this reduction have been clarified, and the right form of the effective self-interaction potential obtained, coinciding with the naive one only at first order.

The resulting system of axion interacting with gravity is described by the Schrodinger-Newton equations and the method suggested by Moroz et al. in [28] has allowed us to solve them numerically for a wide range of different self-interaction potentials.

In the simplest case, without self-interactions, we have confirmed the results from [28] but we have also tested the existence of just this single physically stable branch of solutions by means of the local minimum in the analytical Hamiltonian, obtained through the introduction of diverse ansatzs for the radial part of the axion field in the spherical symmetry case, and by means of the phase diagram, comparing the clump size R_{90} and the number of particles N. The form of this diagram has suggested also the existence of these compact objects for any N value.

The same process have been followed in the case of a single self-interaction term arising by taking just the first order in the naive self-interaction potential. Here our studies coincide with the results obtained by Schiappacasse and Hertzberg in [16], who studied the stability of the solutions by tracking their time evolution. An extra physically unstable bound state solution was obtained besides the stable one. The study of the phase

diagram leads us also to the existence of a maximum number of particles, above which no compact object could be formed.

Afterwards, we analyse the case of a scalar field, with a self-interaction potential as a function of $\phi(x)$ to the fourth power and to the sixth. After the proper non-relativistic reduction and for the right values of the coupling constants, we obtained an effective self-interaction potential formed of two opposite sign terms. This was crucial for the appearance of an extra stable branch of solutions, located in the phase diagram below the unstable branch in R_{90}. This case mimics the dense branch of axions stars in a simplified manner and serves as a warm up for a more complete analysis of the axion self-interaction potential.

Finally, we returned to the axion field case, considering the effective potential deduced directly from axion EFT. In this case all the self-interaction terms appearing in the analytical Hamiltonian share the same sign and we obtained just two extrema in H, a minimum and a maximum, directly related with a physically stable and a physically unstable solutions. This would not have been the case if we had considered the self-interaction potential arising from the naive non-relativistic reduction, whose second order term is in fact of opposite sign. This difference in the sign is directly related with an extra minimum in the analytical Hamiltonian, leading us to the existence of the dense branch of solutions as the one shown in Figure 3.18 which does not appear when the correct axion EFT self-interaction potential is considered.

So, apart from the results and phase diagrams that have just been exposed, something more important and general could be concluded, this is, that the naive non-relativistic reduction, beyond the first order in the power-series expansion of its effective potential, is not able to properly capture the properties of the system. Being more concrete, when the already mentioned naive effective potential was included, it wrongly suggested the existence of a dense branch of solutions even when just a second order term was included, as it has been shown by comparison with the case for the exact effective potential derived from axion EFT. This clearly advises against the use of the naive reduction for this kind of analysis, even more when higher orders of the power-series expansion needs to be considered, as in [31]. This is the main result of our work.

It could be interesting to strengthen these conclusions by employing the non-local field redefinition (3.22) suggested by Namjoo et al. [27], keeping all orders in the power-series expansion of the cosine through an expression similar to (3.104). We leave this for future work.

Bibliography

[1] Peter W Higgs. "Broken symmetries and the masses of gauge bosons". In: *Physical Review Letters* 13.16 (1964), p. 508.

[2] Philip W Anderson. "Plasmons, gauge invariance, and mass". In: *Physical Review* 130.1 (1963), p. 439.

[3] W Noel Cottingham and Derek A Greenwood. *An introduction to the standard model of particle physics*. Cambridge university press, 2007.

[4] Georges Aad et al. "Observation of a new particle in the search for the Standard Model Higgs boson with the ATLAS detector at the LHC". In: *Physics Letters B* 716.1 (2012), pp. 1–29.

[5] Daniel Baumann. "TASI lectures on inflation". In: *arXiv preprint arXiv:0907.5424* (2009).

[6] Alan H Guth. "Inflationary universe: A possible solution to the horizon and flatness problems". In: *Physical Review D* 23.2 (1981), p. 347.

[7] Antonio Riotto. "Inflation and the theory of cosmological perturbations". In: *arXiv preprint hep-ph/0210162* (2002).

[8] Q Shafi and VN Şenoğuz. "Coleman-Weinberg potential in good agreement with wmap". In: *Physical Review D* 73.12 (2006), p. 127301.

[9] Fritz Zwicky. "The redshift of extragalactic nebulae". In: *Helv. Phys. Acta* 6.110 (1933), p. 138.

[10] Sinclair Smith. "The mass of the Virgo cluster". In: *The Astrophysical Journal* 83 (1936), p. 23.

[11] Stacy S McGaugh et al. "The rotation velocity attributable to dark matter at intermediate radii in disk galaxies". In: *The Astrophysical Journal* 659.1 (2007), p. 149.

[12] Douglas Clowe et al. "A direct empirical proof of the existence of dark matter". In: *The Astrophysical Journal Letters* 648.2 (2006), p. L109.

[13] Myungkook James Jee et al. “Discovery of a ringlike dark matter structure in the core of the galaxy cluster Cl 0024+ 17”. In: *The Astrophysical Journal* 661.2 (2007), p. 728.

[14] Jihn E Kim and Gianpaolo Carosi. “Axions and the strong C P problem”. In: *Reviews of Modern Physics* 82.1 (2010), p. 557.

[15] Lawrence Krauss and Michael S Turner. “Quintessence: The Mystery of Missing Mass in the Universe”. In: *PhT* 53.9 (2000), p. 65.

[16] Enrico D Schiappacasse and Mark P Hertzberg. “Analysis of dark matter axion clumps with spherical symmetry”. In: *Journal of Cosmology and Astroparticle Physics* 2018.01 (2018), p. 037.

[17] Stefan Antusch et al. “Oscillons from string moduli”. In: *Journal of High Energy Physics* 2018.1 (2018), pp. 1–42.

[18] Sven Krippendorf, Francesco Muia, and Fernando Quevedo. “Moduli stars”. In: *Journal of High Energy Physics* 2018.8 (2018), pp. 1–53.

[19] Kyohei Mukaida, Masahiro Takimoto, and Masaki Yamada. “On longevity of I-ball/oscillon”. In: *Journal of High Energy Physics* 2017.3 (2017), p. 122.

[20] O Erken et al. “Cosmic axion thermalization”. In: *Physical Review D* 85.6 (2012), p. 063520.

[21] Pierre Sikivie and Q Yang. “Bose-Einstein condensation of dark matter axions”. In: *Physical Review Letters* 103.11 (2009), p. 111301.

[22] Alan H Guth, Mark P Hertzberg, and Chanda Prescod-Weinstein. “Do dark matter axions form a condensate with long-range correlation?” In: *Physical Review D* 92.10 (2015), p. 103513.

[23] Ken’ichi Saikawa and Masahide Yamaguchi. “Evolution and thermalization of dark matter axions in the condensed regime”. In: *Physical Review D* 87.8 (2013), p. 085010.

[24] Roberto D Peccei and Helen R Quinn. “Constraints imposed by CP conservation in the presence of pseudoparticles”. In: *Physical Review D* 16.6 (1977), p. 1791.

[25] Eric Braaten, Abhishek Mohapatra, and Hong Zhang. “Nonrelativistic effective field theory for axions”. In: *Physical Review D* 94.7 (2016), p. 076004.

[26] Eric Braaten, Abhishek Mohapatra, and Hong Zhang. “Classical nonrelativistic effective field theories for a real scalar field”. In: *Physical Review D* 98.9 (2018), p. 096012.

[27] Mohammad Hossein Namjoo, Alan H Guth, and David I Kaiser. “Relativistic corrections to nonrelativistic effective field theories”. In: *Physical Review D* 98.1 (2018), p. 016011.

[28] Irene M Moroz, Roger Penrose, and Paul Tod. "Spherically-symmetric solutions of the Schrödinger-Newton equations". In: *Classical and Quantum Gravity* 15.9 (1998), p. 2733.

[29] Henry Thomas Herbert Piaggio. *An elementary treatise on differential equations and their applications*. G. Bell, 1920.

[30] Joshua Eby et al. "Approximation methods in the study of boson stars". In: *Physical Review D* 98.12 (2018), p. 123013.

[31] Eric Braaten, Abhishek Mohapatra, and Hong Zhang. "Dense axion stars". In: *Physical review letters* 117.12 (2016), p. 121801.

[32] Joshua Eby et al. "Axion stars in the infrared limit". In: *Journal of High Energy Physics* 2015.3 (2015), p. 80.

[33] Luca Visinelli et al. "Dilute and dense axion stars". In: *Physics Letters B* 777 (2018), pp. 64–72.